Structural basis of the filamin A actin-binding domain interaction with F-actin

Daniel V. Iwamoto[1*], Andrew Huehn[2*], Bertrand Simon[1], Clotilde Huet-Calderwood[1], Massimiliano Baldassarre[1,3], Charles V. Sindelar[2]† and David A. Calderwood[1,4]†

[1]Department of Pharmacology, [2]Department of Molecular Biophysics and Biochemistry, [4]Department of Cell Biology, Yale University, New Haven Connecticut, USA. [3]University of Aberdeen Institute of Medical Sciences, Aberdeen, Scotland, UK. *These authors contributed equally to this work. †Corresponding Authors, charles.sindelar@yale.edu, david.calderwood@yale.edu

Abstract

Actin-crosslinking proteins assemble actin filaments into higher-order structures essential for orchestrating cell shape, adhesion and motility. Missense mutations in the tandem calponin homology (CH) domains of their actin-binding domains (ABDs) underlie numerous genetic diseases, but a molecular understanding of these pathologies is hampered by the lack of high-resolution structures of any actin-crosslinking protein bound to F-actin. Here, taking advantage of a high-affinity, disease-associated mutant of the human filamin A (FLNa) ABD, we combine cryo-electron microscopy and functional studies to reveal at near-atomic resolution how the first CH domain (CH1) and residues immediately N-terminal to it engage actin. We further show that reorientation of CH2 relative to CH1 is required to avoid clashes with actin and to expose F-actin-binding residues on CH1. Our data explain localization of disease-associated loss-of-function mutations to FLNaCH1 and gain-of-function mutations to the regulatory FLNaCH2. Sequence conservation argues that this provides a general model for ABD-F-actin binding.

Actin crosslinking proteins mediate assembly of actin filaments into higher-order structures, such as bundles and orthogonal networks, that play essential roles in determining cell morphology and behavior[1,2]. Defects in the actin cytoskeleton underlie numerous genetic diseases, and can arise from missense mutations in the actin-binding domains (ABDs) of these crosslinking proteins[3–5]. Crystal structures of isolated ABDs have shown that they are composed of tandem calponin homology (CH) domains[4–7] but a complete molecular understanding of actin-binding or its perturbation in disease has been hampered by the lack of a high-resolution structure of any actin-crosslinking protein bound to F-actin.

Prior to publication of the first ABD crystal structures, three ABD actin-binding sites (ABS1, ABS2 and ABS3) were predicted based on peptide and fragment binding studies and mutagenesis of a variety of ABDs[8–13]. However, their precise boundaries and relative contributions to F-actin binding were controversial and ABD crystal structures subsequently revealed that the three putative ABSs do not form a continuous surface and include many buried residues[4,7,14]. Indeed, ABS1, which lies in the first helix of CH1, is largely buried at the interface between CH1 and CH2 in the "closed" conformation of the ABD observed in most crystal structures[14–16]. This, together with biophysical experiments and electron microscopy studies of ABDs bound to F-actin[17–22], led to models where inter-domain rearrangement opens the tandem CH domains, exposing CH1 domain actin-binding sites and removing steric clashes between CH2 and actin that would prevent binding. The conformational equilibrium between "closed" and "open" states would thus determine ABD binding to F-actin but the identity of the actin-binding residues and the nature of the conformational changes remained to be determined.

The essential actin-crosslinking protein filamin A (FLNa) is composed of an N-terminal ABD followed by 24 immunoglobulin-like domains, the last of which mediates homodimerization[23]. In addition to crosslinking F-actin, FLNa binds numerous scaffolding, signaling, and transmembrane proteins, and so plays vital roles in the regulation of cell morphology, adhesion, migration, differentiation, and mechanical force-sensing[24,25]. Consistent with these essential roles, nonsense or frameshift mutations in the gene for FLNa, which is on the X chromosome, are typically embryonically lethal in males[3,26]. In heterozygous females, null FLNa mutations cause periventricular nodular heterotopia (PVNH), a neuronal differentiation or migration disorder often also associated with cardiovascular abnormalities[27,28]. Notably, PVNH can also be caused by rare missense mutations that cluster in the FLNaCH1 domain, suggesting that these point mutations result in a loss of function, possibly by disrupting F-actin binding, but this has not been experimentally tested[27,29]. In contrast, missense point mutations in the FLNaCH2 domain are linked to developmental malformations associated with otopalatodigital syndrome spectrum disorders (OPDSD). Unlike PVNH mutations, OPDSD mutations are believed to confer a gain-of-function effect on FLNa[7,30,31] and in the case of the E254K mutation increased affinity for F-actin has been reported[7]. Here, we employed cryo-electron microscopy and biochemical and cellular assays to investigate and characterize the mechanism of ABD binding to F-actin and to rationalize FLNa human disease mutations in molecular detail.

Results

A high-affinity FLNaABD mutant reveals the actin-binding interface at near-atomic resolution

To understand FLNaABD binding to F-actin and potentially explain the molecular basis of disease mutations, we used cryo-electron microscopy (cryo-EM) to visualize the complex between F-actin and a FLNaABD construct encompassing the N-terminal 42 residues plus the tandem CH domains. In initial experiments with wild-type (wt) FLNaABD and phalloidin-stabilized F-actin on an FEI F20 Tecnai electron microscope we were only able to reproduce low-resolution structures similar to those seen in other ABD-F-actin structures and only the CH1 domain was evident[19,22] (**Table 1, Supplementary Fig. 1a, b**). In an attempt to improve ABD decoration of actin filaments and increase resolution, we performed experiments using FLNaABDs containing OPDSD-associated gain-of-function point mutations in FLNaCH2[7]. This yielded 6.6 Å and 7.4 Å resolution maps for the Q170P and E254K mutants respectively (**Table 1, Supplementary Fig. 1a, c, d**). Notably, the FLNaABD-E254K map included density for the CH2 domain, albeit at lower resolution (**Supplementary Fig. 1d**). We therefore used a Titan Krios electron microscope to image FLNaABD-E254K in complex with F-actin, allowing us to approach atomic resolution, resolving both the CH1 domain and F-actin to 3.6 Å resolution (**Fig. 1a, Supplementary Fig. 1a**). The CH2 domain was also visible but again was at lower resolution and is described further in later sections. The F-actin structure in the complex is indistinguishable from previously reported structures of phalloidin-stabilized F-actin (PDB 6C1D, root mean square deviation [RMSD] of Cα atoms in residues T5-C374 is 0.713 Å)[32].

Until now, mapping actin-binding sites (ABS) in ABDs has been contentious; three putative sites (ABS1, 2 and 3) have been proposed but there has been a lack of consensus on the boundaries of these sites and crystallographic data have been unable to reconcile these sites with a continuous binding surface[4,7]. Contrary to prior predictions, our structure reveals that neither the proposed

ABS1 (coarsely mapped to residues 46-56) in helix-A of CH1 nor ABS3 (residues 163-181) in helix-A of the CH2 domain directly engages F-actin. Instead, the ABD binds F-actin through a short sequence immediately N-terminal to the CH1 domain (residues L35-K42) which we term ABS-N, as well as the predicted ABS2 (residues V122-W142) and structurally adjacent residues R91-L104 which were not previously implicated in F-actin binding and which we term ABS2' (**Fig. 1b**). These sites mediate ABD binding in the groove between subdomains 1 and 2 on one actin monomer (*n*) (1348 $Å^2$ of buried surface area) and subdomain 1 on the adjacent (*n+2*) monomer (burying 505 $Å^2$) (**Fig. 1b**).

FLNa residues immediately N-terminal to CH1 contribute to F-actin binding.

Although most of the actin-bound FLNaCH1 domain in our cryo-EM structure closely resembles that of the unbound FLNaABD-E254K crystal structure (PDB 3HOC, RMSD of Cα atoms in residues A39-S149 is 1.094 Å) the first turn of helix-A rearranges to engage F-actin and we can resolve additional N-terminal residues 29-38 which were largely disordered in prior FLNa X-ray structures[6,7] (**Fig. 2a,b**). To test the importance of this region in F-actin binding, we generated a series of N-terminal truncations of C-terminally GFP-tagged FLNaABD constructs (FLNaABD-GFP) and assessed co-localization with F-actin in transfected NIH-3T3 fibroblasts. Briefly, GFP targeting to actin stress fibers was assessed in each GFP-positive cell by a sample-blind observer using an actin targeting score ranging from 1 (no targeting) to 7 (strong targeting); additionally, overall co-localization of GFP and F-actin signals within cells was assessed by calculation of Pearson's Correlation Coefficient (see Methods). Both methods indicated that, whereas loss of amino acids 1-27 or 1-32 had no impact on F-actin co-localization, loss of 1-37 or 1-40 partially inhibited co-localization and loss of 1-44 abrogated it (**Fig. 2c,d Supplementary Fig. 2a,b**) –

implicating residues 33-44, encompassing ABS-N, in F-actin binding. Immunoblotting of cell lysates confirmed that all FLNaABD-GFP constructs were expressed at their expected molecular weights (**Supplementary Fig. 2b**). Of these N-terminal residues, only 37-44 are visible in FLNaABD X-ray crystal structures[6,7], forming the N-terminus of the first α helix (helix-A). In the actin-bound conformation, the N-terminus of helix-A is deformed, moving up to ~3Å (**Fig. 2b**) to engage actin via a probable cation-π interaction between W41 (conserved in the ABD of all filamins and α-actinins, **Supplementary Note**) and actin R28, potentially buttressed by additional interactions with actin F21 and R95 (**Fig. 2e,f**). Mutating W41 inhibited FLNaABD targeting to F-actin in cells (**Fig. 2g,h, Supplementary Fig. 2c,d**), further supporting the importance of this region in actin binding. Moreover, we previously reported that a double K42R,K43R mutation in FLNa helix-A inhibits actin binding[33] and our structure shows that K42 may help stabilize ABS-N (**Fig. 2f**) . Residues N-terminal to helix-A also contribute to actin binding and the importance of hydrophobic contacts between L35 and actin as seen in our structure is supported by the strongly impaired F-actin targeting of an L35A mutant (**Fig. 2g,h, Supplementary Fig. 2c,d**). Together our structural and functional studies firmly establish the biological relevance of ABS-N in ABD-actin binding. Furthermore, despite low sequence conservation of this region, recent biochemical studies on utrophin[34] and a lower-resolution cryo-EM structure of the actin-bound β-III-spectrin ABD[22] indicate a general role of the ABD N-terminus in actin binding.

ABS2' and ABS2 facilitate binding in the groove between adjacent actin subunits

Beyond the ABS-N site, the remaining ABD interface with actin is mediated by ABS2 and ABS2'. ABS2' extends from the middle of the C-E loop into the N-terminus of helix-E and engages both subdomain 2 of the primary interacting actin subunit(*n*) and subdomain 1 of the adjacent

actin(*n+2*) – mainly via hydrophobic and H-bonded interactions (**Fig. 3a**). We validated the importance of these interactions by mutating R91, which is well positioned to form an H-bond with T351 in actin(*n+2*), F99 which contacts I345 in actin (*n+2*), and L104 which is stabilized by CH1-V130 to make a hydrophobic contact with M47 in actin(*n*). R91E, F99A, and L104A mutations each inhibited binding in the cellular F-actin targeting assay (**Fig. 3b,c, Supplementary Fig. 3a**).

ABS2 encompasses part of the E-F loop, the short helix-F and the N-terminal half of helix-G, and engages actin(*n)* subdomains 1 and 2 (**Fig. 3d**). We previously reported that a K135R substitution in ABS2 strongly inhibits actin binding[33] and now show that the K135A mutation has a similar effect (**Fig. 3e,f, Supplementary Fig. 3b**). K135 is highly conserved across all ABDs (**Supplementary Note**) and its sidechain density is directly resolved, indicating potential ionic interactions with actin E93 and D56 (**Fig. 3d**). The importance of ABS2 is further supported by the strong inhibition of F-actin targeting of a charge-reversing lysine mutation at D125, which forms an ionic bond with K61 and potentially H-bonds with Y53 on actin (**Fig. 3d-f, Supplementary Fig. 3b**).

FLNaABD-E254K binds F-actin in an open conformation

Further examination of our structure reveals the necessity for significant CH2 domain reorientation to prevent steric clashes with F-actin upon ABD binding. In our wild-type and OPDSD mutant Q170P structures (**Supplementary Fig. 1a-c**), as well as other published lower-resolution structures[18,19,22], density for the CH2 domain was not evident, consistent with CH2 domain motion in the F-actin-bound form. In contrast, in both our F20 and Krios E254K structures the CH2

domain is apparent, albeit with weaker cryo-EM density and at lower resolution than the rest of the map (**Fig. 4a, Supplementary Fig. 1d**). The lower resolution of this domain again indicates its mobility but was sufficient to reveal that it is oriented outwards and away from actin. Comparison of our actin-bound FLNaABD-E254K structure with the closed conformation seen in the FLNaABD-E254K crystal structure[7] indicates that the closed conformation is incompatible with F-actin binding. As reported previously for α-actinin[19], superposition of the CH1 domains in the actin-bound crystal structures reveals that, in the closed conformation, CH2 would clash with F-actin (**Fig. 4b**). We therefore conclude that an outward movement of the CH2 domain facilitates CH1-mediated binding to actin (**Fig. 4c**). Consistent with this model, isolated FLNaCH1-GFP strongly targeted to F-actin[33] while FLNaCH2-GFP showed no targeting, even with OPDSD mutations Q170P or E254K which otherwise promoted ABD targeting (**Fig. 4d,e, Supplementary Fig. 4a,b**).

In addition to avoiding steric clashes with actin, our structure reveals that CH2 reorientation also exposes a previously-unrecognized and highly-conserved actin-binding residue (W142) at the C-terminus of ABS2. Notably, in unbound FLNaABD crystal structures W142 interacts with H255 in CH2, possibly 'latching' the ABD in a closed conformation (**Fig. 5a**). In contrast, in our actin-bound structure, this interaction is replaced by hydrophobic contacts between W142 and actin (**Fig. 5b**), and a W142A mutation inhibited targeting to F-actin in cells (**Fig. 5c,d, Supplementary Fig. 4c**). These data argue that W142 plays a regulatory role by binding either CH2 in a closed inhibitory state, or F-actin in the open active conformation. In α-actinin-4, the homologous W147 may serve a similar role by engaging K255 in CH2. Consistent with this, K255 mutations that presumably unlatch the ABD and increase affinity for F-actin are associated with the kidney

disease focal segmental glomerulosclerosis[35]. Indeed, disease-associated gain-of-function mutations are found throughout the CH2 domain of FLNa and other ABDs including in its hydrophobic core (**Supplementary Note**). Purified OPDSD-associated mutant FLNaABDs (Q170P or E254K) analyzed by scanning fluorimetry exhibited sharp melting points at lower temperatures than wild-type FLNaABD, indicative of altered stability (**Fig. 5e**). Consistent with their enhanced F-actin targeting (**Fig. 4d,e, Supplementary Fig. 4a,b**), OPDSD-associated ABD mutants also displayed increased affinity for F-actin in co-sedimentation assays (**Fig. 5f,g, Supplementary Fig. 4d**). We hypothesize that OPDSD mutations destabilize the CH2 domain in the closed ABD position and shift the conformational equilibrium in favor of ABD opening, facilitating CH1-mediated F-actin binding.

Filamin A CH1 domain disease mutations confer loss of function

In addition to the gain-of-function CH2 domain mutations that cause OPDSD, mutations in FLNa are also linked to the neuronal migration disorder PVNH[27]. Most FLNa PVNH mutations are nonsense and frameshift resulting in the loss of FLNa protein[3,27]. However, rare PVNH-associated missense mutations that cluster in the FLNaCH1 domain are also seen, and result in phenotypically similar, albeit somewhat milder, disease[27]. We propose that these mutations, many of which are found in the ABS-N, ABS2 and ABS2' (**Supplementary Note**), disrupt the actin-binding interface and cause a loss-of-function. Consistent with this, the PVNH mutations A39G and A128V strongly impaired FLNaABD targeting to F-actin in cells (**Fig. 6a,b, Supplementary Fig. 5a**) and F-actin binding in *in vitro* co-sedimentation assays (**Fig. 6c,d, Supplementary Fig. 4d**). Our ability to purify soluble recombinant FLNaABD mutants with size-exclusion chromatography profiles consistent with monomeric protein (**Supplementary Fig. 5b)** argues that the mutations do not

result in general misfolding. This conclusion is supported by their sharp melting points in differential scanning fluorimetry experiments (**Fig. 6e**). Notably, despite a wild-type melting point and elution profile (**Fig 6e**, **Supplementary Fig. 5b**), indicating that FLNaABD A39G is properly folded, it does not appear to bind actin with the 1:1 ratio seen for the wild-type and other gain- and loss-of-function mutations (**Fig 6c, Supplementary Fig. 4d**). This suggests an anomalous binding mechanism. We propose that A39 (in ABS-N) normally stabilizes the actin-binding residue W41 (**Fig. 2e,f**). While loss of this stabilization is likely to account for the observed reduction in binding affinity, it is difficult to envisage how it also alters stoichiometry of binding, either by occluding adjacent binding sites or by altering F-actin conformation. As this low-occupancy low-affinity interaction is not conducive to structural analysis we cannot currently explain the reduced stoichiometry of FLNaABD A39G. For a second PVNH mutation, A128V, we note that A128 does not make direct contact with F-actin but packs tightly behind the main interacting surface of ABS2 (helix-F). An A128V substitution would perturb this surface (**Supplementary Fig. 5c**), likely explaining its disruption of actin binding and possibly contributing to the decrease in thermal stability seen in scanning fluorimetry experiments (**Fig. 6e**). Our structure also allows us to rationalize the previously unexplained M102V PVNH-associated mutation which lies in ABS2' and inhibited F-actin binding in cells (**Fig. 6a,b, Supplementary Fig. 5a**). M102, in conjunction with F99, extends towards I345 of actin(*n+2*) (**Fig. 3a**) and substitution with the shorter valine likely prevents this interaction. Two other PVNH-associated FLNa mutations that lie outside the actin-binding interface (E82V and S149F) had little or no effect on F-actin targeting, producing only modestly reduced actin-targeting scores but no reduction in Pearson's correlation coefficient (**Fig. 6a,b, Supplementary Fig. 5a,d**), and the basis for their clinical effects remains unclear. Additional FLNaCH1 domain PVNH mutations also occur in ABS2. The V122 side chain is

wedged between H87 and H88 of actin(*n*) and a V122G mutation strongly inhibited association with F-actin (**Fig. 6a,b, Supplementary Fig. 5a**). The K127N severely inhibited actin targeting, and in our structure K127 is in range to make an ionic bond with E167 in actin(*n+2*) (**Fig. 6a,b, Supplementary Fig 5a**). Notably, disease-associated mutations in the ABD of FLNc and α-actinin-2 also localize to regions corresponding to FLNa ABS2[36,37] (**Supplementary Note**). Mutations at I119 inhibited F-actin binding (**Fig. 6a,b, Supplementary Fig. 5a**), probably due to disruption of the hydrophobic core of CH1, and α-actinin-1 and -2 also contain disease-associated mutations in this region[38,39].

Discussion

Our high-resolution cryo-EM structure of FLNaABD-E254K bound to F-actin provides a detailed foundation for understanding the molecular basis of actin binding by tandem CH domains, revealing several new features of the ABD-actin binding mechanism. We show that upon actin binding, FLNa residues immediately N-terminal to the CH1 domain become ordered and contribute to F-actin binding. By identifying three actin-binding sites (ABS-N, ABS2' and ABS2) we resolve controversy surrounding the specific sites involved in F-actin binding. We find that ABS-N participates in hydrophobic and potential cation-π interactions with subdomain 1 of actin while ABS2' binds an adjacent F-actin subunit. The previously mapped ABS2 also makes key ionic and hydrophobic interactions. The functional importance of each of these sites was validated using structure-guided mutations. Our structure also indicates CH2 domain movement associated with actin-binding, establishing that, as previously proposed based on earlier lower-resolution structures[18,19,22], binding involves ABD opening and does not involve direct CH2-actin interactions. In addition to avoiding steric clashes of the CH2 domain with actin, ABD opening

exposes the highly-conserved actin-binding residue W142 in ABS2 which, in the closed conformation, binds the CH2 domain, serving as a regulatory latch to stabilize the closed ABD. Finally, combining cellular and biochemical analysis of disease-associated FLNaABD mutations with our structural studies helps explain the localization of PVNH disease-associated loss-of-function point mutations to the actin-binding CH1 domain and gain-of-function OPDSD mutations to the regulatory CH2 domain.

The N-terminal flanking regions of ABDs are diverse in length and sequence, but the ABS-N sequence is conserved in filamins and α-actinins (**Supplementary Note**) and, despite relatively low sequence similarity with the FLNa N-terminus, deletion of residues 1-27 in utrophin ABD or 1-51 in β-III-spectrin ABD has been shown to dramatically reduce F-actin binding[22,34]. Thus, residues N-terminal to CH1 have functionally conserved biological significance in multiple ABDs.

Notably, at least in the case of FLNa, residues preceding ABS-N are not necessary for actin binding as N-terminal truncations (Δ1-27 and Δ1-32) did not diminish ABD co-localization with F-actin. Consistent with this, an alternate FLNa transcript that results in initiation at M28 (equivalent to our Δ1-27 ABD) produces functional FLNa protein that targets to F-actin[40]. Furthermore, FLNb also has a relatively short N-terminus (equivalent to the Δ1-27 FLNaABD) and the FLNbABD binds F-actin with affinities comparable to the FLNaABD in the present study[41]. This suggests that the variability in sequence N-terminal to ABS-N may provide mechanisms to regulate ABD binding to actin. Indeed, calmodulin binding to N-terminal residues of plectin has been proposed to regulate plectin interactions with F-actin[42,43]. Calmodulin has also been reported to inhibit FLNa binding to F-actin[44] but, rather than binding the N-terminal region, calmodulin was proposed to

utilize a cryptic binding site (residues 87-96) in the FLNaCH1 domain that became exposed upon F-actin binding. We now show that the proposed calmodulin-binding site faces away from F-actin and we observe no substantial conformational changes in this site upon F-actin binding, making it unclear how calmodulin would selectively bind this region in the FLNaABD-F-actin complex to drive dissociation. Furthermore, despite the strong sequence and structural conservation between FLNa and FLNb, calmodulin did not inhibit FLNb binding to F-actin[41]. The structural basis for any effect of calmodulin on FLNa binding to F-actin therefore remains to be determined.

FLNa binding to F-actin is however clearly influenced by the CH2 domain and our structural data show that when bound to F-actin the FLNaABD domain adopts an "open" position distinct from the closed conformations seen in FLNaABD crystal structures[6,7]. However, even in the F-actin-bound FLNaABD E254K structure, the lower resolution of the CH2 domain reveals that this domain is mobile and this presumably explains why it was not visible in most other ABD-actin complexes[19,22]. An open conformation is necessary to avoid steric clashes with actin and to expose the otherwise occupied F-actin binding residue W142 in ABS2. Notably, W142 plays alternative functional roles by either binding F-actin when the ABD is in an open conformation or binding CH2 in the closed unbound conformation. W142 is completely conserved across ABDs (**Supplementary Note**) and has been implicated in latching α-actinin-4[35] and plectin[45] closed, indicating that this switching mechanism may be conserved mechanism for controlling the conformational equilibrium of many, if not all, tandem CH ABDs.

Our cellular and biochemical studies demonstrate loss-of-actin binding with most of the human PVNH mutations that localize to FLNaCH1. While some appear to disrupt direct molecular

interactions with F-actin (M102V, V122G, K127N), others likely elicit their effects by deforming actin-binding sites or the CH1 domain in general (A39G, I119D, A128V). Conversely, we propose that the FLNaABD exists in a conformational equilibrium in solution and that the gain-of-function OPDSD mutations in the CH2 domain exert their effects by shifting that equilibrium towards open states. The decreased melting temperature and increased affinity of FLNaABD-E254K and -Q170P for F-actin (this report and [7]) are consistent with this model but solution dynamics experiments, as recently applied to the β-III-spectrin ABD[22], will be required to test it further. Notably, the FLNaABD is apparently also dynamic even when bound to F-actin, and this motility presumably accounts for the lower resolution (or lack of resolution) of the CH2 domain in actin-bound structures[19,22], and suggests that there may be many "open" conformations compatible with actin binding.

In conclusion, our work provides structural and functional insight into the ramifications of FLNa disease mutations and resolves substantial controversies in mapping the actin-binding sites of tandem CH domains.

Accession Codes

Cryo-EM reconstructions were deposited in the Electron Microscopy Data Bank with the following accession numbers: F20-F-actin-FLNaABD 7833, F20-F-actin-FLNaABD-Q170P 7832, F20-F-actin-FLNaABD-E254K 8918, and Krios-F-actin-FLNaABD-E254K 7831. The corresponding FLNaABD-E254K filament model was deposited in the Protein Data Bank with accession number 6D8C.

Acknowledgements

We thank Z. Razinia for generating numerous FLNa constructs, S. Wu for expertise in using the Krios microscope, J. Lees for advice on model refinement, and M. Lemmon for helpful comments in preparing the manuscript. We also thank the Yale Center for Research Computing for guidance and use of the Farnam Cluster, as well as the staff at the YMS Center for Molecular Imaging for the use of the EM Core Facility. This work was funded by grants from the National Institutes of Health [R01-GM068600 (D.A.C.), R01-NS093704 (D.A.C.), R37-GM057247 (C.V.S.), R01-GM110530 (C.V.S.), T32-GM007324, T32-GM008283] and an award from American Heart Association 15PRE25700119 (D.V.I).

Author Contributions

D.V.I., M.B., and D.A.C. conceived the project. D.V.I., B.S., C.H.C., and M.B. designed constructs and collected and interpreted biochemical and cellular data. A.H. and D.V.I. prepared cryo-EM samples and collected cryo-EM data. A.H. and C.V.S. performed cryo-EM analysis and model refinement. D.V.I, A.H., C.V.S., and D.A.C. wrote the manuscript with contributions from all other authors.

Competing Financial Interests Statement

The authors declare no competing interests.

References

1. Pollard, T. D. Actin and Actin-Binding Proteins. *Cold Spring Harb. Perspect. Biol.* **8,** 575–591 (2016).
2. Svitkina, T. The Actin Cytoskeleton and Actin-Based Motility. *Cold Spring Harb. Perspect. Biol.* **10,** 1–22 (2018).
3. Robertson, S. P. Filamin A: Phenotypic diversity. *Curr. Opin. Genet. Dev.* **15,** 301–307 (2005).
4. Sjöblom, B., Ylänne, J. & Djinović-Carugo, K. Novel structural insights into F-actin-binding and novel functions of calponin homology domains. *Curr. Opin. Struct. Biol.* **18,** 702–708 (2008).
5. Gimona, M., Djinovic-Carugo, K., Kranewitter, W. J. & Winder, S. J. Functional plasticity of CH domains. *FEBS Lett.* **513,** 98–106 (2002).
6. Ruskamo, S. & Ylänne, J. Structure of the human filamin A actin-binding domain. *Acta Crystallogr. Sect. D Biol. Crystallogr.* **65,** 1217–1221 (2009).
7. Clark, A. R., Sawyer, G. M., Robertson, S. P. & Sutherland-Smith, A. J. Skeletal dysplasias due to filamin A mutations result from a gain-of-function mechanism distinct from allelic neurological disorders. *Hum. Mol. Genet.* **18,** 4791–4800 (2009).
8. Bresnick, A. R., Warren, V. & Condeelis, J. Identification of a Short Sequence Essential for Actin Binding by Dictyostelium ABP-120. *J. Biol. Chem.* **265,** 9236–9240 (1990).
9. Levine, B. A., Moir, A. J. G., Patchell, V. B. & Perry, S. V. The interaction of actin with dystrophin. *FEBS Lett.* **263,** 159–162 (1990).
10. Karinch, A. M., Zimmer, W. E. & Goodman, S. R. The identification and sequence of the actin-binding domain of human red blood cell beta spectrin. *J. Biol. Chem.* **265,** 11833–11840 (1990).
11. Levine, B., Moir, A., Patchell, V. & Perry, S. Binding sites involved in the interaction of actin with the N-terminal region of dystrophin. *FEBS Lett.* **298,** (1992).
12. Hemmings, L., Kuhlman, P. A. & Critchley, D. R. Analysis of the actin-binding domain of alpha-actinin by mutagenesis and demonstration that dystrophin contains a functionally homologous domain. *J. Cell Biol.* **116,** 1369–1380 (1992).

13. Corrado, K., Mills, P. & Chamberlain, J. Deletion analysis of the dystrophin-actin binding domain. *FEBS Lett.* **344,** 255–260 (1994).

14. Goldsmith, S. C. *et al.* The structure of an actin-crosslinking domain from human fimbrin. *Nat. Struct. Biol.* **4,** 708–712 (1997).

15. Keep, N. H. *et al.* Crystal structure of the actin-binding region of utrophin reveals a head-to-tail dimer. *Structure* **7,** 1539–1546 (1999).

16. Norwood, F. L. M., Sutherland-Smith, A. J., Keep, N. H. & Kendrick-Jones, J. The structure of the N-terminal actin-binding domain of human dystrophin and how mutations in this domain may cause Duchenne or Becker muscular dystrophy. *Structure* **8,** 481–491 (2000).

17. Liu, J., Taylor, D. W. & Taylor, K. A. A 3-D reconstruction of smooth muscle α-actinin by CryoEm reveals two different conformations at the actin-binding region. *J. Mol. Biol.* **338,** 115–125 (2004).

18. Galkin, V. E., Orlova, A., Cherepanova, O., Lebart, M.-C. & Egelman, E. H. High-resolution cryo-EM structure of the F-actin-fimbrin/plastin ABD2 complex. *Proc. Natl. Acad. Sci. U. S. A.* **105,** 1494–1498 (2008).

19. Galkin, V. E., Orlova, A., Salmazo, A., Djinovic-Carugo, K. & Egelman, E. H. Opening of tandem calponin homology domains regulates their affinity for F-actin. *Nat. Struct. Mol. Biol.* **17,** 614–6 (2010).

20. Lin, A. Y., Prochniewicz, E., James, Z. M., Svensson, B. & Thomas, D. D. Large-scale opening of utrophin's tandem calponin homology (CH) domains upon actin binding by an induced-fit mechanism. *Proc. Natl. Acad. Sci. U. S. A.* **108,** 12729–33 (2011).

21. Broderick, M. J. F., Bobkov, A. & Winder, S. J. Utrophin ABD binds to F-actin in an open conformation. *FEBS Open Bio* **2,** 6–11 (2012).

22. Avery, A. W. *et al.* Structural basis for high-affinity actin binding revealed by a beta-III-spectrin SCA5 missense mutation. *Nat. Commun.* **8,** 1–7 (2017).

23. Nakamura, F., Osborn, T. M., Hartemink, C. a., Hartwig, J. H. & Stossel, T. P. Structural basis of

filamin A functions. *J. Cell Biol.* **179,** 1011–1025 (2007).

24. Razinia, Z., Mäkelä, T., Ylänne, J. & Calderwood, D. A. Filamins in Mechanosensing and Signaling. *Annu. Rev. Biophys.* **41,** 227–246 (2012).

25. Nakamura, F., Stossel, T. P. & Hartwig, J. H. The filamins: Organizers of cell structure and function. *Cell Adhes. Migr.* **5,** 160–169 (2011).

26. Sheen, V. L. *et al.* Mutations in the X-linked filamin 1 gene cause periventricular nodular heterotopia in males as well as in females. *Hum. Mol. Genet.* **10,** 1775–83 (2001).

27. Parrini, E. *et al.* Periventricular heterotopia : phenotypic heterogeneity and correlation with Filamin A mutations. *Brain* **72,** 1892–1906 (2006).

28. Chen, M. H. *et al.* Thoracic aortic aneurysm in patients with loss of function Filamin A mutations: Clinical characterization, genetics, and recommendations. *Am. J. Med. Genet.* **176A,** 337–350 (2018).

29. Solé, G. *et al.* Bilateral periventricular nodular heterotopia in France: Frequency of mutations in FLNA, phenotypic heterogeneity and spectrum of mutations. *J. Neurol. Neurosurg. Psychiatry* **80,** 1394–1398 (2009).

30. Robertson, S. P. Otopalatodigital syndrome spectrum disorders: otopalatodigital syndrome types 1 and 2, frontometaphyseal dysplasia and Melnick-Needles syndrome. *Eur. J. Hum. Genet. EJHG* **15,** 3–9 (2007).

31. Robertson, S. P. *et al.* Localized mutations in the gene encoding the cytoskeletal protein filamin A cause diverse malformations in humans. *Nat. Genet.* **33,** 487–491 (2003).

32. Mentes, A. *et al.* High-resolution cryo-EM structures of actin-bound myosin states reveal the mechanism of myosin force sensing. *PNAS* **115,** 1292–1297 (2018).

33. Razinia, Z., Baldassarre, M., Cantelli, G. & Calderwood, D. A. ASB2α, an E3 ubiquitin ligase specificity subunit, regulates cell spreading and triggers proteasomal degradation of filamins by targeting the filamin calponin homology 1 domain. *J. Biol. Chem.* **288,** 32093–32105 (2013).

34. Singh, S. M., Bandi, S. & Mallela, K. M. G. The N-Terminal Flanking Region Modulates the

Actin Binding Affinity of the Utrophin Tandem Calponin-Homology Domain. *Biochemistry* **56,** 2627–2636 (2017).

35. Weins, A. *et al.* Disease-associated mutant alpha-actinin-4 reveals a mechanism for regulating its F-actin-binding affinity. *Proc. Natl. Acad. Sci. U. S. A.* **104,** 16080–16085 (2007).

36. Valdés-Mas, R. *et al.* Mutations in filamin C cause a new form of familial hypertrophic cardiomyopathy. *Nat. Commun.* **5,** 5326 (2014).

37. Bagnall, R. D., Molloy, L. K., Kalman, J. M. & Semsarian, C. Exome sequencing identifies a mutation in the ACTN2 gene in a family with idiopathic ventricular fibrillation, left ventricular noncompaction, and sudden death. *BMC Med. Genet.* **15,** 99 (2014).

38. Kunishima, S. *et al.* ACTN1 mutations cause congenital macrothrombocytopenia. *Am. J. Hum. Genet.* **92,** 431–438 (2013).

39. Theis, J. L. *et al.* Echocardiographic-determined septal morphology in Z-disc hypertrophic cardiomyopathy. *Biochem. Biophys. Res. Commun.* **351,** 896–902 (2006).

40. Jenkins, Z. A. *et al.* Differential regulation of two FLNA transcripts explains some of the phenotypic heterogeneity in the loss-of-function filaminopathies. *Hum. Mutat.* **39,** 103–113 (2018).

41. Sawyer, G. M., Clark, A. R., Robertson, S. P. & Sutherland-Smith, A. J. Disease-associated Substitutions in the Filamin B Actin Binding Domain Confer Enhanced Actin Binding Affinity in the Absence of Major Structural Disturbance: Insights from the Crystal Structures of Filamin B Actin Binding Domains. *J. Mol. Biol.* **390,** 1030–1047 (2009).

42. Kostan, J., Gregor, M., Walko, G. & Wiche, G. Plectin isoform-dependent regulation of keratin-integrin α6β4 anchorage via Ca2+/calmodulin. *J. Biol. Chem.* **284,** 18525–18536 (2009).

43. Song, J. G. *et al.* Structural insights into Ca2+-calmodulin regulation of plectin 1a-integrin β4 interaction in hemidesmosomes. *Structure* **23,** 558–570 (2015).

44. Nakamura, F., Hartwig, J. H., Stossel, T. P. & Szymanski, P. T. Ca2+ and Calmodulin Regulate the Binding of Filamin A to Actin Filaments. *J. Biol. Chem.* **280,** 32426–32433 (2005).

45. García-Alvarez, B., Bobkov, A., Sonnenberg, A. & De Pereda, J. M. Structural and functional analysis of the actin binding domain of plectin suggests alternative mechanisms for binding to F-actin and integrin β4. *Structure* **11,** 615–625 (2003).

Figure Legends

Figure 1. Cryo-EM map and model of FLNaABD-E254K bound to F-actin. a The cryo-EM map (left and middle) has been filtered to 3.6 Å resolution, masked to illustrate the actin and FLNaCH1 region, and fit with computationally refined models (right) for actin (different subunits in dark blue, cyan, and light blue) and the FLNaCH1 domain (green). Phalloidin (orange) and Mg.ADP (grey) were resolved within F-actin. **b** The binding interface of the FLNaABD (green ribbon) consists of the N-terminal actin-binding site ABS-N (pink), actin-binding site 2 (ABS2, yellow) and the ABS2 extension (ABS2', red), which makes contacts with actin subunits (*n*) (dark blue, surface representation) and (*n+2*) (light blue, surface representation) on actin subdomains 1 and 2 (SD1 and SD2, labeled in grey).

Figure 2. **ABS-N contributes to F-actin binding. a** Cryo-EM density depicting ABS-N (residues P29-K43, pink) extending from helix-A of the FLNaCH1 domain (green) alongside actin(*n*) (dark blue). **b** Superposition of the refined actin-bound FLNaCH1 and ABS-N (green, pink) cryo-EM structure and the published unbound FLNaCH1 crystal structure PDB 3HOC (red) illustrates the formation of the structured ABS-N upon actin-binding. Actin in surface representation and FLNa in ribbon representation, colored as in (**a**). **c** F-actin targeting of wild-type (wt) and N-terminal deletion constructs of FLNaABD-GFP expressed in mouse NIH-3T3 fibroblasts. Bars = mean ± SEM, n = number of scored cells from 3 independent experiments, * significantly different from

wt ($P<0.001$) in a one-way ANOVA ($F_{6,944}=211$) with Dunnett's multiple comparisons test. **d** Pearson's correlation coefficient (PCC) scoring of FLNaABD-GFP co-localization with N-terminal truncations. Center = median, boxes = 25^{th}-50^{th} and 50^{th}-75^{th} percentiles, whiskers extend to 10^{th} and 90^{th} percentiles, n = number of scored cells from 3 independent experiments, * significantly different from wt ($P<0.001$) in a one-way ANOVA ($F_{6,711}=21.63$) with Dunnett's multiple comparisons test. **e** Detailed view of actin-binding by ABS-N with binding residues in stick representation. **f** Cryo-EM density supports a probable cation-π interaction between FLNa W41 and actin R28. **g** F-actin targeting of ABS-N-mutant FLNaABD-GFP, scored and graphed as in (**c**). One-way ANOVA ($F_{3,564}=339.9$) with Dunnett's multiple comparisons test. **h** PCC scoring of ABS-N-mutant FLNaABD-GFP, scored and graphed as in (**d**). One-way ANOVA ($F_{3,410}=13$) with Dunnett's multiple comparisons test.

Figure 3. **ABS2 and ABS2' facilitate major binding interactions with F-actin. a** Detailed view of the FLNa ABS2' (green) binding interface with the actin(*n+2*) subunit (light blue) and actin(*n*) (dark blue). **b** F-actin targeting scores of ABS2'-mutant FLNaABD-GFP. Bars = mean ± SEM, n = number of scored cells from 3 independent experiments, * significantly different from wt ($P<0.001$) in a one-way ANOVA ($F_{4,670}=286.6$) with Dunnett's multiple comparisons test. **c** PCC scoring of ABS2'-mutant FLNaABD-GFP. Center = median, boxes = 25^{th}-50^{th} and 50^{th}-75^{th} percentiles, whiskers extend to 10^{th} and 90^{th} percentiles, n = number of scored cells from 3 independent experiments, * significantly different from wt ($P<0.001$ unless otherwise specified) in a one-way ANOVA ($F_{4,585}=11.41$) with Dunnett's multiple comparisons test. **d** Detailed view of the FLNa ABS2 (green) binding interface with the actin(*n+2*) subunit (light blue) and actin(*n*) (dark blue). **e** F-actin targeting scores of ABS2-mutant FLNaABD-GFP, scored and graphed as in

(**b**). n=number of scored cells from at least 3 independent experiments, one-way ANOVA ($F_{3,568}$=308.5) with Dunnett's multiple comparisons test. **f** PCC scoring of ABS2-mutant FLNaABD-GFP, scored and graphed as in (**c**). n=number of scored cells from at least 3 independent experiments, one-way ANOVA ($F_{3,491}$=16.75) with Dunnett's multiple comparisons test.

Figure 4. **Opening of the ABD is required to avoid steric clashes and facilitate actin binding.** **a** Low-pass filtered (10 Å resolution) map of FLNaABD-E254K bound to F-actin. FLNaCH2 from the FLNaABD crystal structure (PDB 3HOC) was independently rigid-body docked into additional density (tan, right). **b, c** The FLNaABD crystal structure is superimposed onto the actin-bound cryo-EM structure to align CH1 domains. Instances of steric clash between the crystallographic CH2 domain (purple) and F-actin cryo-EM density are indicated by red arrows (**b**). Repositioning of the CH2 domain from the closed crystalized form (purple) into its open actin-bound form (tan) is depicted with an arrow (**c**). **d** Actin-targeting scores of FLNa-ABD, -CH1, or -CH2-GFP with OPDSD mutations. Bars = mean ± SEM, n = number of scored cells from at least 3 independent experiments, * significantly different from wt ($P<0.001$) in a one-way ANOVA ($F_{7,1576}$=1894) with Dunnett's multiple comparisons test. **e** PCC scoring of FLNa-ABD, -CH1, or -CH2-GFP with OPDSD mutations. Center = median, boxes = 25^{th}-50^{th} and 50^{th}-75^{th} percentile, whiskers extend to 10^{th} and 90^{th} percentiles, n = number of scored cells from 3 independent experiments, * significantly different from wt ($P<0.001$) in a one-way ANOVA ($F_{7,1283}$=258.7) with Dunnett's multiple comparisons test.

Figure 5. ABD opening is mediated by an inter-CH domain latch. a FLNaABD crystal structure showing the W142-H255 cation-π interaction that may latch the CH1 (red) and CH2 (purple) domains closed. **b** Actin-bound FLNaCH1 (green) reveals W142 interaction with actin (dark blue). In the closed CH2 conformation (purple) H255 would clash with actin. **c** F-actin targeting score of the W142A mutant FLNaABD-GFP. Bars = mean ± SEM, n = number of scored cells from 4 independent experiments, * significantly different from wt ($P<0.001$) in a one-way ANOVA ($F_{2,529}=757$) with Dunnett's multiple comparisons test. **d** PCC scoring of the W142A-mutant FLNaABD-GFP. Center = median, boxes = 25^{th}-50^{th} and 50^{th}-75^{th} percentile, whiskers extend to 10^{th} and 90^{th} percentiles, n = number of scored cells from 4 independent experiments, * significantly different from wt ($P<0.001$) in a one-way ANOVA ($F_{2,424}=28.1$) with Dunnett's multiple comparisons test. **e** Triplicate derivative melting curves from differential scanning fluorimetry for purified wt, Q170P, and E254K FLNaABDs indicate a single melting temperature peak for each protein: wt = 48.1 ± 0.6 °C, Q170P = 40.1 ± 0.8 °C, E254K = 39.3 ± 0.5 °C (± SD). **f** Left, representative Coomassie-stained actin co-sedimentation assay gels containing pellet (top) or supernatant (bottom) samples with no-actin controls (middle) for purified wt, Q170P, and E254K FLNaABDs. Uncropped gel images are shown in **Supplementary Data Set 1**. On the right, assay data points were plotted to generate a binding curve to calculate an apparent dissociation constant (K_d). **g** Apparent K_d was averaged for each ABD from at least six co-sedimentation assays. Bars = mean ± SEM, n = number of independent co-sedimentation assays, * significantly different from wt in an unpaired two-tailed t-test (wt vs. Q170P, $t=2.501$, $df=14$, $P=0.0254$; wt vs. E254K, $t=4.086$, $df=14$, $P=0.0011$) (see also **Supplementary Fig. 4d**).

Figure 6. FLNaCH1 domain mutations confer a loss-of-function to F-actin binding. a F-actin targeting scores of periventricular nodular heterotopia disease mutant FLNaABD-GFP. Bars = mean ± SEM, n=number of scored cells from at least 3 independent experiments, n = number of scored cells from at least 3 independent experiments, * significantly different from wt ($P<0.001$) in a one-way ANOVA ($F_{9,1680}=227.5$) with Dunnett's multiple comparisons test. **b** PCC scoring of periventricular nodular heterotopia disease mutant FLNaABD-GFP. Center = median, boxes = 25^{th}-50^{th} and 50^{th}-75^{th} percentile, whiskers extend to 10^{th} and 90^{th} percentiles, n = number of scored cells from at least 3 independent experiments, * significantly different from wt ($P<0.001$) in a one-way ANOVA ($F_{9,1234}=27.64$) with Dunnett's multiple comparisons test. **c** Left, representative Coomassie-stained actin co-sedimentation assay gels containing pellet (top) or supernatant (bottom) samples with no-actin controls (middle) for purified wt, A39G, and A128V FLNaABDs. Uncropped gel images are shown in **Supplementary Data Set 1**. On the right, assay data points were plotted to generate a binding curve to calculate an apparent dissociation constant (K_d). **d** Apparent K_d was averaged for FLNaABD-wt, -A39G, or -A128V protein from at least four assays (wt here is the same as appears in **Fig. 5g** for comparison purposes). Bars = Mean ± SEM, n = number of independent co-sedimentation assays, * significantly different from wt in an unpaired two-tailed t-test (wt vs. A39G, $t=4.163$, $df=13$, $P=0.0011$; wt vs. A128V, $t=5.934$, $df=12$, $P<0.0001$) (see also **Supplementary Fig. 4d**). **e** Triplicate derivative melting curves from differential scanning fluorimetry for purified wt, A39G, and A128V FLNaABDs indicate a single melting temperature peak for each protein (wt here is the same as appears in **Fig. 5e** for comparison purposes): wt = 48.1 ± 0.6 °C, A39G = 47.3 ± 0.5 °C, A128V = 42.0 ± 0.9 °C (± SD).

Table 1. Cryo-EM data collection, refinement and validation statistics

	Krios-ABD-E254K (EMDB-7831, PDB 6D8C)	F20-ABD-E254K (EMDB-8918)	F20-ABD-Q170P (EMDB-7832)	F20-ABD-wt (EMDB-7833)
Data collection and processing				
Magnification	37500	40096	40096	40096
Voltage (kV)	300	200	200	200
Electron exposure (e^{-}/Å^2)	51	46-53	60	47
Defocus range (μm)	1.0 – 2.9	1.1 – 2.7	1.1 – 2.7	1.1 – 2.7
Pixel size (Å)	1.33	1.247	1.247	1.247
Symmetry imposed	27.54 Å rise -166.73˚ twist	27.67 Å rise -166.89˚ twist	27.52 Å rise -166.88˚ twist	None
Initial particle images (no.)	~450,000	28,000	20,000	75,000
Final particle images (no.)	67,000	28,000	20,000	24,000
Map resolution (Å)	3.54	7.4	6.6	9.8
FSC threshold	0.143	0.143	0.143	0.143
Map resolution range (Å)	3.3 – 5.2	5.1 – 8.6	5.3 – 7.8	6.2 – 10.2
Refinement				
Initial model used (PDB code)	3HOC, 6C1D ChEBI:8040			
Model resolution (Å)	3.76			
FSC threshold	0.500			
Model resolution range (Å)	3.76 – 45			
Map sharpening *B* factor (Å^2)	-150			
Model composition				
Nonhydrogen atoms	19665			
Protein residues	2455			
Ligands	5 Mg.ADP, 3 phalloidin			
B factors (Å^2)				
Protein	49.91			
Ligand	42.24			
R.m.s. deviations				
Bond lengths (Å)	0.005			
Bond angles (°)	1.071			
Validation				
MolProbity score	1.65			
Clashscore	9.19			
Poor rotamers (%)	0.71			
Ramachandran plot				
Favored (%)	97.08			
Allowed (%)	2.92			
Disallowed (%)	0			

Online Methods

Reagents and DNA constructs

Polyclonal anti-GFP (#600-101-215, Rockland), anti-vinculin (V9131, Sigma-Aldrich), secondary anti-goat-680RD (#926-68074, LI-COR), secondary anti-mouse 800CW (#925-32212, LI-COR), and Alexafluor-568-phalloidin (Life Technologies) were purchased. Polyclonal anti-human FLNa antibody, which cross-reacts with mouse FLNa, was raised in rabbits[46,47]. 1 mg/ml fibronectin solution was purchased (#F1141, Sigma). Human FLNa-ABD and -CH domain constructs in a pcDNA3 vector with a C-terminal GFP tag have been described previously[33,48,49]. FLNa mutations were generated by QuikChange site-directed mutagenesis (Stratagene). For bacterial expression, select FLNa-ABD constructs were also subcloned into a modified pET32-6xHis vector using KpnI and EcoRI restriction sites to generate N-terminally His-tagged FLNaABD.

Cell culture

Mouse NIH3T3 cells were obtained from Yale colleagues and tested negative for mycoplasma contamination. Cells were cultured in DMEM (#11965, GIBCO) with 9% bovine serum (#16170078, GIBCO) and penicillin/streptomycin (#15140122, GIBCO), and incubated at 37 °C in a humidified atmosphere containing 5% CO_2. To express FLNa constructs, 8×10^4 cells/well were plated in a 6-well dish and 24 h later were transfected with 1.5 µg plasmid DNA using PEI (#23966-1, Polysciences Inc).

Actin Filament Targeting and Microscopy

Transfected cells were plated on coverslips previously coated with 5 µg/mL fibronectin and cultured for 24 h. Cells were washed with PBS and then fixed and permeabilized in cold 4% paraformaldehyde + 0.1% Triton X-100 in cytoskeletal buffer (10 mM MES, pH6.1, 150 mM NaCl, 5 mM EGTA, 5 mM $MgCl_2$, 5 mM glucose) for 30 min at room temperature. Coverslips were washed with PBS and incubated in cytoskeletal buffer containing 0.2% bovine serum albumin (BSA), 50 mM NH_4Cl, and 0.3% Triton X-100 for 1 h at room temperature, then incubated for 1 h at room temperature with Alexafluor-568-Phalloidin in the same buffer and washed in PBS. Coverslips were mounted onto glass slides using ProLong Diamond Antifade Mountant (#P36965, Invitrogen). Microscopy images of transfected cells expressing comparable levels of GFP were acquired using a Nikon Eclipse Ti microscope with a 100x objective using Micro-Manager software[50] and analyzed in ImageJ (National Institutes of Health, Bethesda, rsb.info.nih.gov). To quantify GFP-tagged FLNaABD targeting to actin filaments, co-localization of GFP and phalloidin-568 signal was scored on a scale of 1 (low overlap) to 7 (high overlap) in a sample-blind manner. To avoid potential bias in assigning co-localization scores, GFP and phalloidin-568 signal images were also subjected to an automated CellProfiler co-localization function[51] to normalize images and calculate the Pearson's Correlation Coefficient (PCC) between the two images. Images were excluded from automated PCC scoring if the field contained non-expressing or multiple cells. In all cases the expression of the GFP-tagged FLNa construct at the predicted molecular weight was confirmed by immunoblotting against GFP, while vinculin was used as a loading control.

Protein Purification

6xHis-tagged FLNaABD DNA constructs were expressed in Rosetta strain *E. coli* and induced with 500 µM IPTG for 18 h at 16 °C. Bacterial cultures were pelleted and resuspended in lysis buffer (20 mM Tris pH 7.9, 500 mM NaCl, 5 mM imidazole, 1 mM PMSF, 1% Triton X-100, 700 µg/mL Lysozyme, 6.4 µg/mL DNAse1) at 4 °C. 6xHis-tagged proteins were purified over Ni-NTA beads (#70666 Novagen), eluted with 400 mM imidazole, and dialyzed into co-sedimentation assay buffer (50 mM Tris pH 8.0, 150 mM KCl, 2 mM $MgCl_2$, 0.01% Triton X-100, 5 mM DTT). Proteins were further purified by size-exclusion chromatography (SEC) on a Superdex200 Prep Grade column (GE Healthcare), then concentrated using a 10 kDa MWCO centrifugal filter unit (#UFC801024, Millipore), flash frozen in liquid nitrogen, and stored at -80 °C until use. Purified proteins remained monomeric after concentration and freezing as seen in SEC (data not shown).

Actin Co-sedimentation Assays

Actin, purified from chicken breast into G buffer (2 mM Tris pH8, 200 µM ATP, 5 mM DTT, 100 µM $CaCl_2$) and stored at -80 °C until use, was a gift from the Koleske lab (Yale)[52]. 1 µM G-actin was polymerized with 20 mM imidazole, 150 mM KCl, 2 mM EGTA, 4 mM DTT, and 2 mM $MgCl_2$ for 30 min at room temperature and stabilized with 1 µM phalloidin. Polymerized actin was titrated with a range of FLNaABD concentrations in co-sedimentation assay buffer, incubated at room temperature for 1 h, and spun at 270,000 × g in a Beckman TLA-100 rotor. Supernatants were collected, and protein pellets were washed with co-sedimentation assay buffer then resuspended in water. 30% of the supernatant sample and 100% of the pellet sample were loaded for SDS-PAGE separation. Gels were stained with Coomassie Blue, destained, and scanned for densitometry using the Odyssey Infrared Imaging system (LI-COR). No-actin control ABD band intensities were subtracted from the corresponding co-sedimented ABD bands to remove F-actin-

independent sedimentation signal and divided by the intensity of the actin to normalize for F-actin loading. Data points were fitted to a one-site binding model in Prism software (GraphPad) to calculate apparent binding affinity and stoichiometry[53].

Differential Scanning Fluorimetry

His-tagged FLNaABD thermal stability was determined by differential scanning fluorimetry with SYPRO orange[54] (#S6650, Invitrogen) using a CFXConnect Real-Time PCR Detection System (BioRad). 30 µM ABD in co-sedimentation assay buffer was mixed with SYPRO orange and heated from 4 °C to 95 °C in 1 °C increments over 2 h. Data were collected in triplicate wells using the FAM filter from three independent experiments. Melting temperatures were calculated from the first derivative of the melting curve using the BioRad CFX Manager software.

Cryo-Electron Microscopy Sample Preparation and Data Collection

Purified 6xHis-FLNaABD-wt, -Q170P, or -E254K were incubated at 60 µM with 15 µM phalloidin-stabilized F-actin in a low salt co-sedimentation assay buffer (described above) at least 30 minutes before freezing. The Q170P and E254K samples were diluted 1:1 in H_2O immediately prior to freezing. Samples were prepared using holey carbon grids (Quantifoil R1.2/1.3 Micro Tools GmbH, Grosslöbichau, Germany) and a manual plunger device. Micrographs data sets were collected on a 200-kV FEI Tecnai F20 electron microscope equipped with a Gatan K2 Summit direct electron-counting camera at a pixel size of 1.247 Å. Micrographs were recorded in 0.3 second sub-frames over 7.2-10.2 seconds for a total dose of 47-60 $e^-/Å^2$ over a nominal defocus range of 1.1–2.7 µm. Later, a separate data set on the E254K sample was collected on a 300-kV Titan Krios microscope equipped with an energy filter and a Gatan K2 Summit camera in super-

resolution mode at a physical pixel size of 1.33 Å. Micrographs were recorded in 0.25 second sub-frames over 12 seconds for a total dose of 50 $e^-/Å^2$ over a nominal defocus range of 1.0–2.9 µm.

3D Refinement

Micrographs were aligned and dose-corrected using MotionCor2[55], where sub-frame motion correction (3x3 array) was applied to the wt and Tecnai F20 E254K data sets, while the Krios E254K data set was binned by 2. The Krios E254K data set was corrected for magnification distortion using parameters estimated by mag_distortion_estimate[56]. Contrast transfer function parameters were calculated using Gctf[57], and micrographs where Gctf did not detect signal at resolutions better than <4 Å were excluded from structural refinement for the Krios E254K data set. Filaments were manually selected using *e2helixboxer* from the EMAN software package[58] and extracted at a spacing of ~27.5 Å. The wt, Q170P, and E254K data sets collected on the Tecnai F20 used a box size of 390 pixels, while the Krios E254K data set used a box size of 210 pixels. Structure refinement was performed using IHRSR single-particle helical processing[59,60] as implemented in RELION (version 2.0.3)[61,62]. The first round of refinement employed masks generated from earlier refinements that were low-pass filtered to 60 Å and included 10-20 Å soft edges using the *relion_mask_create* tool. The Tecnai F20 E254K and Q170P data sets were further processed in a second round of refinement using a mask generated from the 7 central actin subunits and CH1 domains that were low-pass filtered to 60 Å and included 15 Å soft edges. The Krios E254K data set was also improved in a second round of refinement using a helical mask generated from the results of the first round of refinement but constrained to the central 30% Z-slice, low-pass filtered to 60 Å, and included 6.5 Å soft edges. The wt data was subjected to a particle subtraction and masked 3D classification approach described elsewhere[63] to determine occupancy

674 at the single subunit level. The decorated class (~33% particles) was then restored to its
675 unsubtracted state and further refined using the same mask as earlier in the first round of
676 refinement.
677
678 The resolution and B-factor of the final maps were calculated from the FSC correlation of
679 independent half-maps in postprocessing with RELION following gold standard protocols
680 (**Supplementary Fig. 1a**). Symmetry was first imposed in real space on the independent half maps
681 in the Tecnai F20 E254K (27.67 Å rise, -166.89° twist), Q170P (27.52 Å rise, -166.88˚ twist), and
682 Krios E254K (27.54 Å rise, -166.73˚ twist) data sets using the *relion_helix_toolbox* command. The
683 imposed helical parameters were derived from local searches of symmetry on the full map in
684 RELION. The FSC calculations for the Tecnai F20 E254K and Q170P data sets used a mask
685 generated from earlier refinements that was thresholded to contain only actin subunits and CH1
686 domains, low-pass filtered to 20 Å, and included 15 Å soft edges. The resolution of the Tecnai F20
687 E254K map reach 7.4 Å, while the Q170P map reached 6.6 Å. The symmetrized Krios E254K
688 volume was used to generate a mask that included only actin and the CH1 domains, was low-pass
689 filtered to 15 Å, and included 8 Å soft edges. This mask was next used in postprocessing
690 calculations, where the final Krios E254K map reached a resolution of 3.6 Å. The final
691 symmetrized Krios E254K map is low-pass filtered to 3.6 Å and sharpened with a B-factor of -
692 150. The FSC calculations for the wt data set used the same mask from its structural refinement,
693 and reached a resolution of 9.8 Å. The resolution ranges of each map were estimated using *blocres*
694 from the Bsoft software package[64].
695
696 **Model Building, Refinement, and Validation**

PDB models of phalloidin-stabilized F-actin (PDB ID 6C1D, chain B, residues 1-375)[32] and FLNa CH1 (PDB ID 3HOC, chain A, residues 39-153)[7] were first fit as rigid bodies into the final symmetrized Krios E254K map using UCSF Chimera[65]. This model was refined against the final map in Phenix[66] using real space refinement with simulated annealing. Next, the model was refined by manual adjustments and all molecule real-space refinement with Ramachandran restraints in Coot[67] and real-space refinement in Phenix without simulated annealing. After several iterations, additional N-terminal FLNa residues were built by the N-terminal addition of residues into the cryo-EM density in Coot and followed by real-space refinement in Phenix. Multiple subunits and phalloidin subunits (PDB ID 6C1D) were loaded into the neighboring densities and evaluated in MolProbity[68] for steric clashes, which were manually fixed in Coot. Next, structural data for phalloidin (ChEBI ID 8040)[69] was used to generate geometric restraints in eLBOW[70] for real-space refinement with the final map in phenix. The refined phalloidin chains were combined with the model. The final model was evaluated by MolProbity and data statistics are given in **Table 1**. Cation-π interactions were investigated using the CaPTURE program[71]. Structural figures were generated in ChimeraX[72].

Statistics and Reproducibility

For cellular F-actin co-localization experiments, each GFP-tagged FLNa construct or GFP alone was tested in at least three independent transfections, with at least 25 image pairs collected for each construct per experiment for quantification. Actin-targeting scores or PCC scores from imaged cells for each construct were averaged and compared to FLNaABD-wt by one-way ANOVA ($P<0.0001$ for all ANOVAs) with Dunnett's multiple comparisons test; precise values for n, F and degrees of freedom are listed in the relevant figures and legends. For co-sedimentation

assays, each 6xHis-tagged FLNa protein was tested in at least four independent assays, and average apparent K_d of each mutant FLNaABD was compared to wt with an unpaired two-tailed t-test; precise values for n, t, P and degrees of freedom are listed in the relevant figures and legends. For differential scanning fluorimetry, average melting temperature of each mutant FLNaABD was compared to wt from triplicate wells of three independent experiments by one-way ANOVA ($F_{4,40}$=339.1, P<0.0001) with Dunnett's multiple comparisons test.

Data availability

Cryo-EM reconstructions were deposited in the Electron Microscopy Data Bank with the following accession numbers: F20-F-actin-FLNaABD 7833, F20-F-actin-FLNaABD-Q170P 7832, F20-F-actin-FLNaABD-E254K 8918, and Krios-F-actin-FLNaABD-E254K 7831. The corresponding FLNaABD-E254K filament model was deposited in the Protein Data Bank with accession number 6D8C. Source data for F-actin targeting analyses (**Figs. 2c,d,g,h, 3b,c,e,f, 4d,e, 5c,d,** and **6a,b**) and co-sedimentation assays (**Figs. 5g** and **6d**) are available with the paper online. Other data are available from the corresponding author upon reasonable request.

Methods References

46. Kiema, T. *et al.* The molecular basis of filamin binding to integrins and competition with talin. *Mol. Cell* **21,** 337–347 (2006).

47. Heuzé, M. L. *et al.* ASB2 targets filamins A and B to proteasomal degradation. *Blood* **112,** 5130–5140 (2008).

48. Lad, Y. *et al.* Structure of three tandem filamin domains reveals auto-inhibition of ligand binding. *EMBO J.* **26,** 3993–4004 (2007).

49. Razinia, Z. *et al.* The E3 ubiquitin ligase specificity subunit ASB2α targets filamins for

744 proteasomal degradation by interacting with the filamin actin-binding domain. *J. Cell Sci.* **124,**
745 2631–2641 (2011).
746 50. Edelstein, A., Amodaj, N., Hoover, K., Vale, R. & Stuurman, N. Computer control of microscopes
747 using μmanager. *Curr. Protoc. Mol. Biol.* 1–17 (2010). doi:10.1002/0471142727.mb1420s92
748 51. Carpenter, A. E. *et al.* CellProfiler: Image analysis software for identifying and quantifying cell
749 phenotypes. *Genome Biol.* **7,** R100 (2006).
750 52. MacGrath, S. M. & Koleske, A. J. Arg/Abl2 modulates the affinity and stoichiometry of binding
751 of cortactin to F-actin. *Biochemistry* **51,** 6644–6653 (2012).
752 53. Heier, J. A., Dickinson, D. J. & Kwiatkowski, A. V. Measuring Protein Binding to F-actin by Co-
753 sedimentation. *J. Vis. Exp.* **123,** 1–8 (2017).
754 54. Boivin, S., Kozak, S. & Meijers, R. Optimization of protein purification and characterization using
755 Thermofluor screens. *Protein Expr. Purif.* **91,** 192–206 (2013).
756 55. Zheng, S. Q. *et al.* MotionCor2: anisotropic correction of beam-induced motion for improved
757 cryo-electron microscopy. *Nat. Methods* **14,** 331–332 (2017).
758 56. Grant, T. & Grigorieff, N. Automatic estimation and correction of anisotropic magnification
759 distortion in electron microscopes. *J. Struct. Biol.* **192,** 204–208 (2015).
760 57. Zhang, K. Gctf: Real-time CTF determination and correction. *J. Struct. Biol.* **193,** 1–12 (2016).
761 58. Tang, G. *et al.* EMAN2: An extensible image processing suite for electron microscopy. *J. Struct.*
762 *Biol.* **157,** 38–46 (2007).
763 59. Egelman, E. H. Reconstruction of helical filaments and tubes. *Methods Enzymol.* **482,** 167–183
764 (2010).
765 60. Egelman, E. H. A robust algorithm for the reconstruction of helical filaments using single-particle
766 methods. *Ultramicroscopy* **85,** 225–234 (2000).
767 61. He, S. & Scheres, S. H. W. Helical reconstruction in RELION. *J. Struct. Biol.* **198,** 163–176
768 (2017).
769 62. Scheres, S. H. W. RELION: Implementation of a Bayesian approach to cryo-EM structure

determination. *J. Struct. Biol.* **180,** 519–530 (2012).

63. Huehn, A. *et al.* The actin filament twist changes abruptly at boundaries between bare and cofilin-decorated segments. *J. Biol. Chem.* **293,** 5377–5383 (2018).

64. Cardone, G., Heymann, J. B. & Steven, A. C. One number does not fit all: Mapping local variations in resolution in cryo-EM reconstructions. *J. Struct. Biol.* **184,** 226–236 (2013).

65. Pettersen, E. F. *et al.* UCSF Chimera - A visualization system for exploratory research and analysis. *J. Comput. Chem.* **25,** 1605–1612 (2004).

66. Adams, P. D. *et al.* PHENIX: A comprehensive Python-based system for macromolecular structure solution. *Acta Crystallogr. Sect. D Biol. Crystallogr.* **66,** 213–221 (2010).

67. Emsley, P., Lohkamp, B., Scott, W. G. & Cowtan, K. Features and development of Coot. *Acta Crystallogr. Sect. D Biol. Crystallogr.* **66,** 486–501 (2010).

68. Chen, V. B. *et al.* MolProbity: All-atom structure validation for macromolecular crystallography. *Acta Crystallogr. Sect. D Biol. Crystallogr.* **66,** 12–21 (2010).

69. Hastings, J. *et al.* ChEBI in 2016: Improved services and an expanding collection of metabolites. *Nucleic Acids Res.* **44,** D1214–D1219 (2016).

70. Moriarty, N. W., Grosse-Kunstleve, R. W. & Adams, P. D. Electronic ligand builder and optimization workbench (eLBOW): A tool for ligand coordinate and restraint generation. *Acta Crystallogr. Sect. D Biol. Crystallogr.* **65,** 1074–1080 (2009).

71. Gallivan, J. P. & Dougherty, D. A. Cation-pi interactions in structural biology. *Proc. Natl. Acad. Sci.* **96,** 9459–9464 (1999).

72. Goddard, T. D. *et al.* UCSF ChimeraX: Meeting modern challenges in visualization and analysis. *Protein Sci.* **27,** 14–25 (2018).

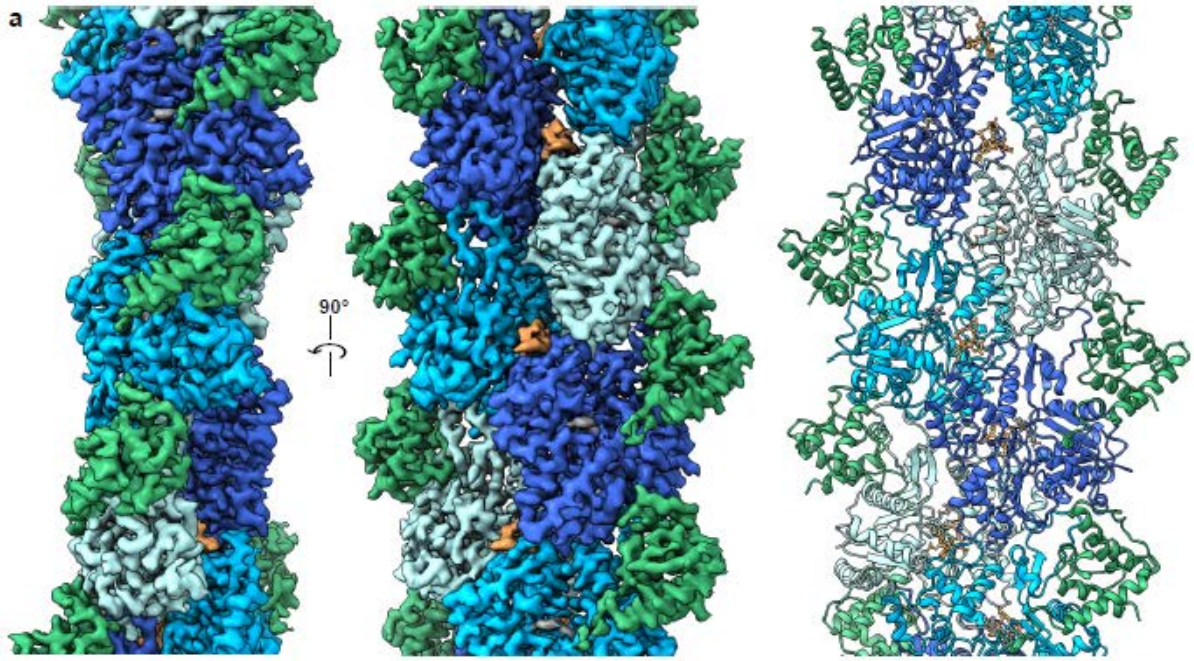
a
90°

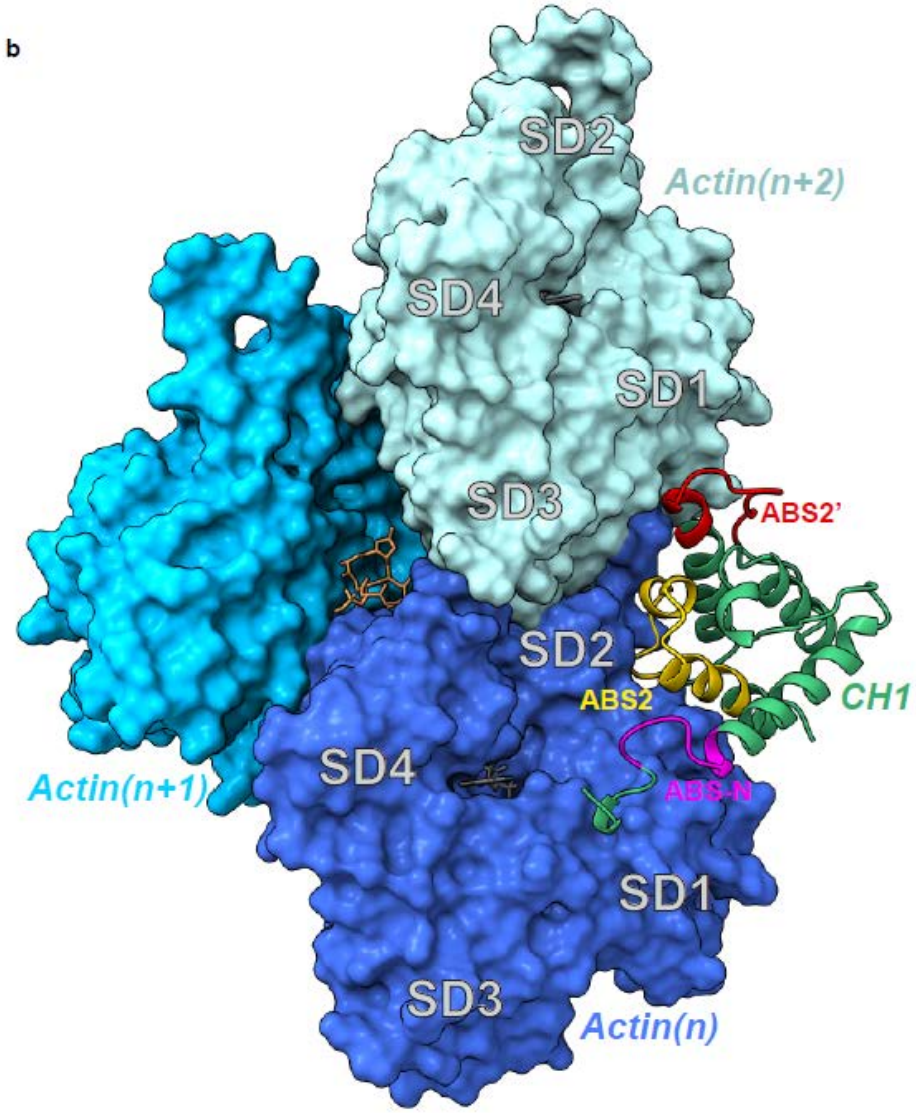
b
SD2
Actin(n+2)
SD4
SD1
SD3
ABS2'
SD2
ABS2
CH1
SD4
ABS-N
Actin(n+1)
SD1
SD3
Actin(n)

Figure 1.

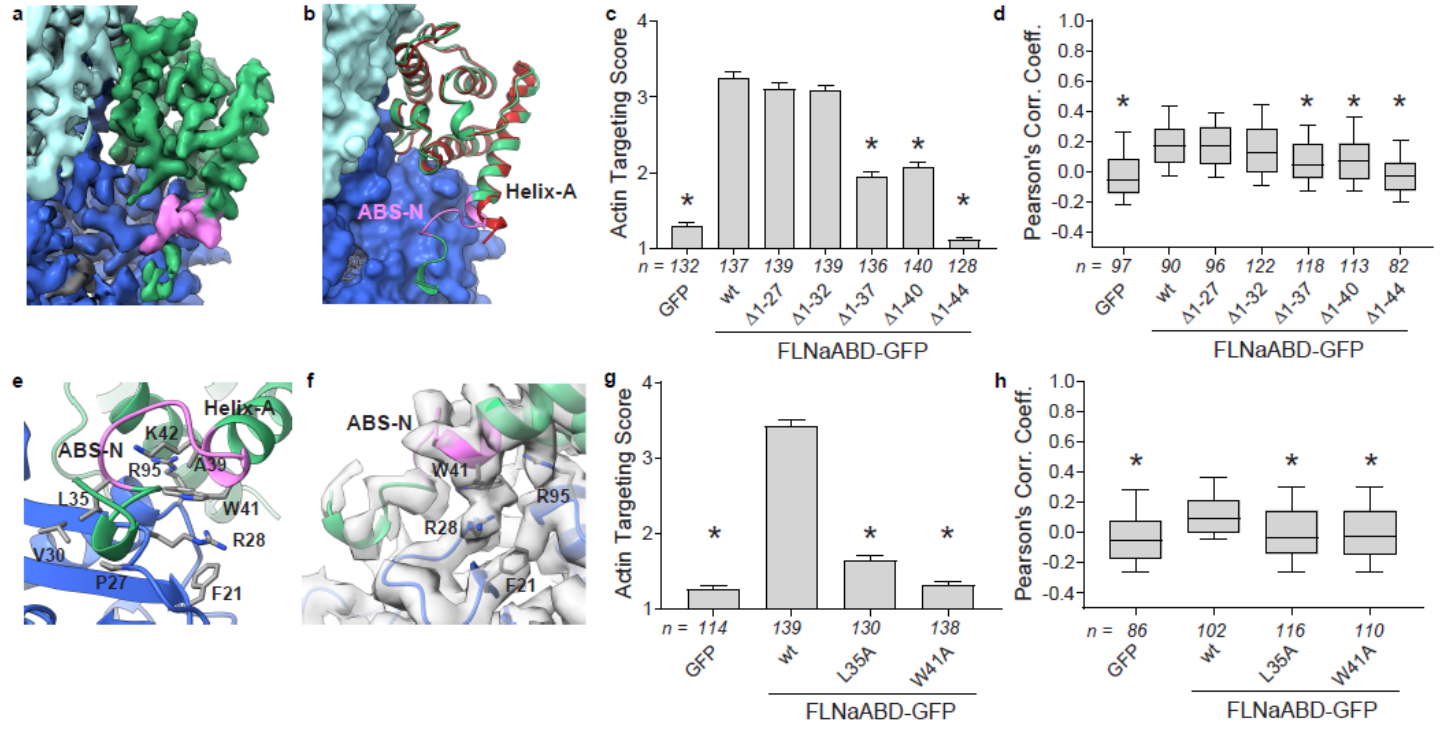
a
b
ABS-N
Helix-A
c
Actin Targeting Score
n = 132 137 139 139 136 140 128
GFP
wt
Δ1-27
Δ1-32
Δ1-37
Δ1-40
Δ1-44
FLNaABD-GFP
d
Pearson's Corr. Coeff.
n = 97 90 96 122 118 113 82
GFP
wt
Δ1-27
Δ1-32
Δ1-37
Δ1-40
Δ1-44
FLNaABD-GFP
e
Helix-A
ABS-N
K42
R95
A39
L35
W41
R28
V30
P27
F21
f
ABS-N
W41
R95
R28
F21
g
Actin Targeting Score
n = 114 139 130 138
GFP
wt
L35A
W41A
FLNaABD-GFP
h
Pearson's Corr. Coeff.
n = 86 102 116 110
GFP
wt
L35A
W41A
FLNaABD-GFP

Figure 2.

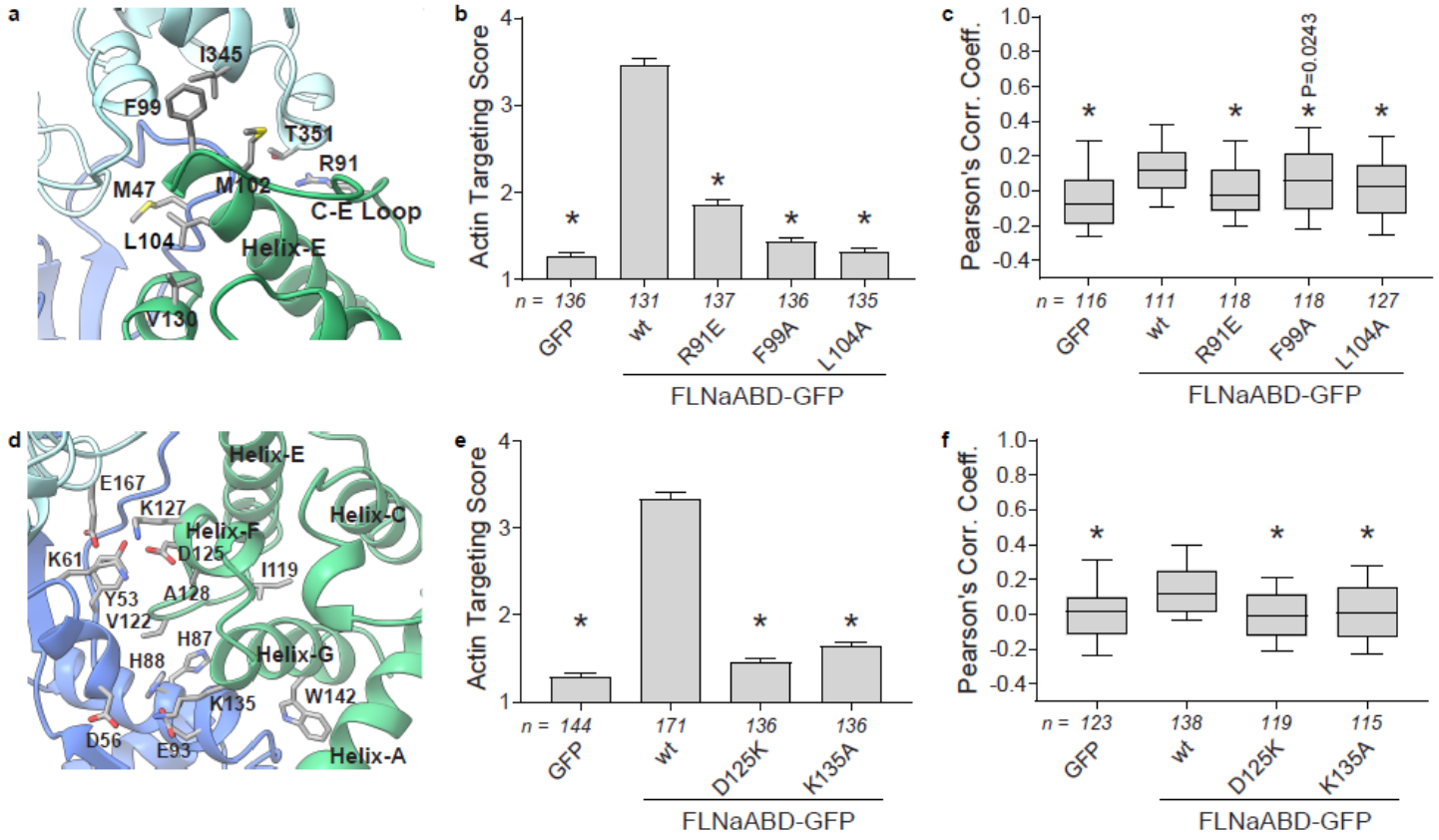
a
I345
F99
T351
R91
M47
M102
C-E Loop
L104
Helix-E
V130
b
Actin Targeting Score
n = 136 131 137 136 135
GFP
wt
R91E
F99A
L104A
FLNaABD-GFP
c
Pearson's Corr. Coeff.
P=0.0243
n = 116 111 118 118 127
GFP
wt
R91E
F99A
L104A
FLNaABD-GFP
d
Helix-E
E167
K127
Helix-F
Helix-C
D125
K61
I119
A128
Y53
V122
H87
H88
Helix-G
K135
W142
D56
E93
Helix-A
e
Actin Targeting Score
n = 144 171 136 136
GFP
wt
D125K
K135A
FLNaABD-GFP
f
Pearson's Corr. Coeff.
n = 123 138 119 115
GFP
wt
D125K
K135A
FLNaABD-GFP

Figure 3.

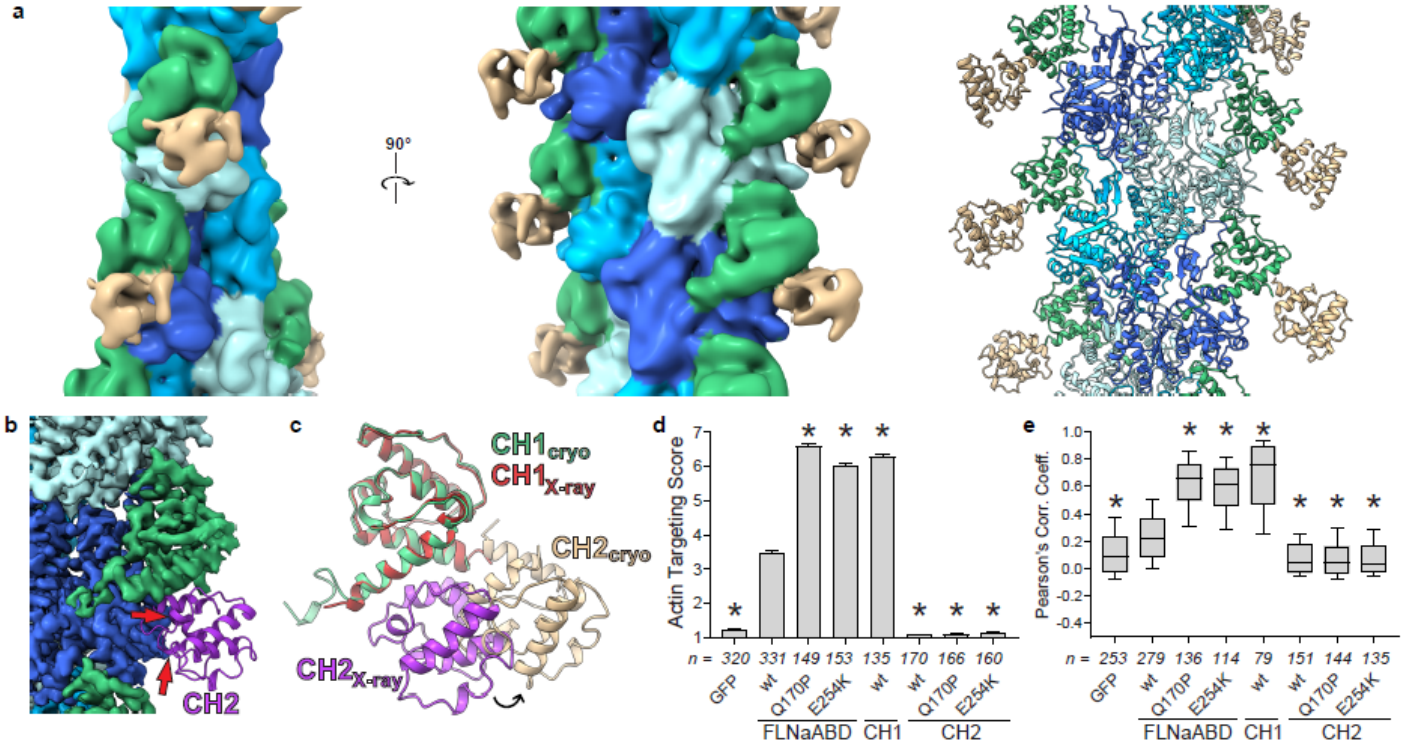
a
90°
b
CH2
c
CH1cryo
CH1X-ray
CH2cryo
CH2X-ray
d
Actin Targeting Score
n = 320 331 149 153 135 170 166 160
GFP
wt
Q170P
E254K
wt
wt
Q170P
E254K
FLNaABD
CH1
CH2
e
Pearson's Corr. Coeff.
n = 253 279 136 114 79 151 144 135
GFP
wt
Q170P
E254K
wt
wt
Q170P
E254K
FLNaABD
CH1
CH2

Figure 4.

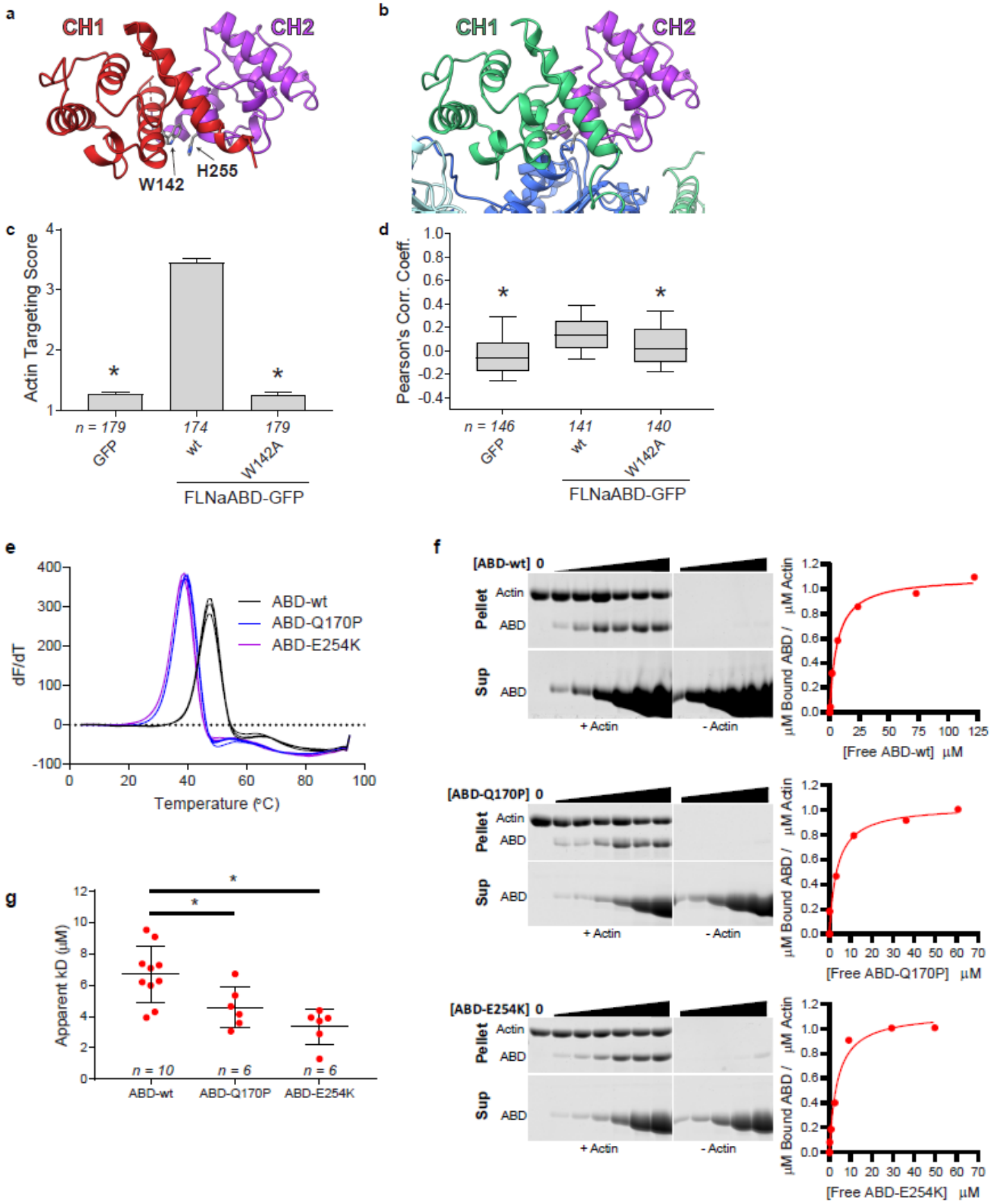
a
CH1
CH2
W142
H255
b
CH1
CH2
c
Actin Targeting Score
n = 179
174
179
GFP
wt
W142A
FLNaABD-GFP
d
Pearson's Corr. Coeff.
n = 146
141
140
GFP
wt
W142A
FLNaABD-GFP
e
dF/dT
Temperature (°C)
ABD-wt
ABD-Q170P
ABD-E254K
f
[ABD-wt] 0
[ABD-Q170P] 0
[ABD-E254K] 0
Pellet
Sup
Actin
ABD
+ Actin
- Actin
µM Bound ABD / µM Actin
[Free ABD-wt] µM
[Free ABD-Q170P] µM
[Free ABD-E254K] µM
g
Apparent kD (µM)
n = 10
n = 6
n = 6
ABD-wt
ABD-Q170P
ABD-E254K

Figure 5.

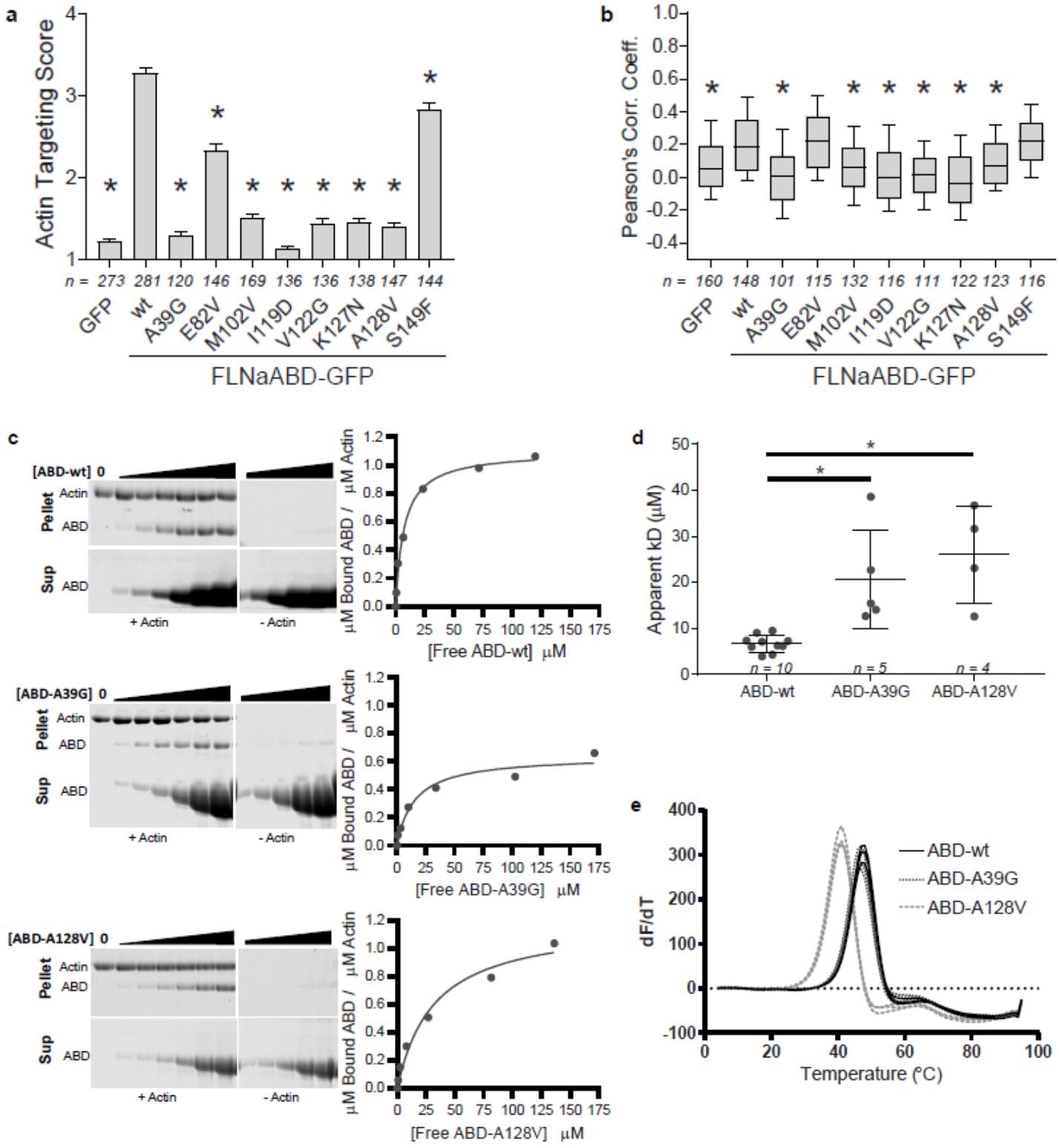
a
Actin Targeting Score
n = 273 281 120 146 169 136 136 138 147 144
GFP wt A39G E82V M102V I119D V122G K127N A128V S149F
FLNaABD-GFP
b
Pearson's Corr. Coeff.
n = 160 148 101 115 132 116 111 122 123 116
GFP wt A39G E82V M102V I119D V122G K127N A128V S149F
FLNaABD-GFP
c
[ABD-wt] 0
Pellet Actin ABD
Sup ABD
+ Actin - Actin
µM Bound ABD / µM Actin
[Free ABD-wt] µM
[ABD-A39G] 0
[Free ABD-A39G] µM
[ABD-A128V] 0
[Free ABD-A128V] µM
d
Apparent kD (µM)
n = 10 n = 5 n = 4
ABD-wt ABD-A39G ABD-A128V
e
dF/dT
ABD-wt
ABD-A39G
ABD-A128V
Temperature (°C)

Figure 6.

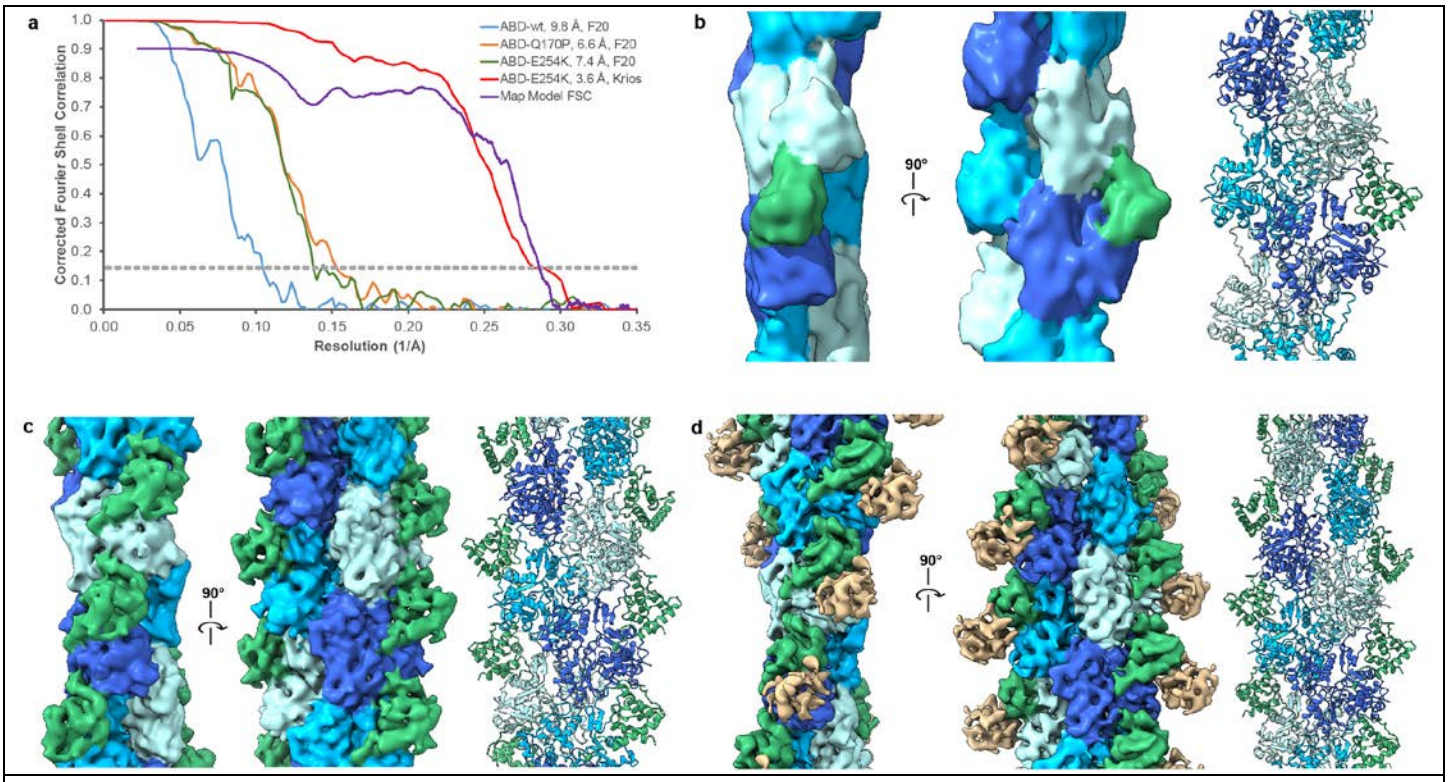

Supplementary Figure 1.

FLNaABD-F-actin complexes.

a High frequency noise-substituted Fourier shell correlation calculations between independently refined half maps reveals the resolution of each map. The FSC curve between the final FLNaABD-E254K-F-actin map and refined model is shown in purple. **b** A 10 Å-filtered cryo-EM density map of the wild-type (wt) FLNaABD (left and middle) was rigid-body docked with crystal structures for actin (PDB 6C1D, different subunits in dark blue, cyan, and light blue) and FLNaCH1 (PDB 3HOP, green) (right). **c** A 6.6 Å-filtered cryo-EM density map of the gain-of-function mutant FLNaABD-Q170P (left and middle) was docked with the refined actin and FLNaCH1 models (right) and colored as in (**b**). **d** A 7.4 Å-filtered cryo-EM density map of the gain-of-function mutant FLNaABD-E254K (left and middle) was docked with the refined actin and FLNaCH1 models (right) and colored as in (**b**). Observed extra density for FLNaCH2 is shown in tan.

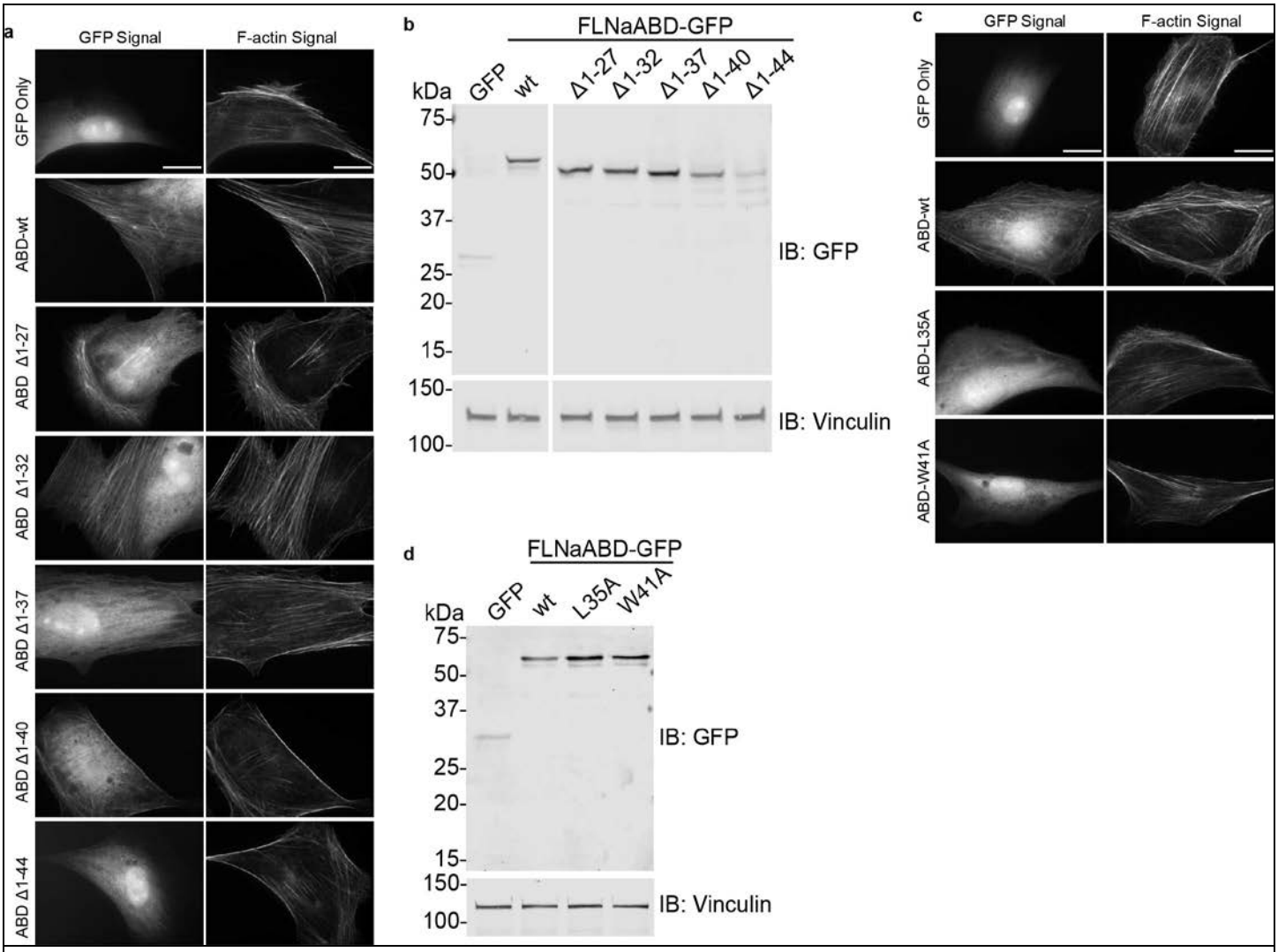

Supplementary Figure 2

ABS-N mutations inhibit FLNaABD-F-actin binding.

a Micrographs of mouse NIH-3T3 fibroblasts transiently transfected with GFP or FLNaABD-GFP ± N-terminal truncation constructs after fixation, permeabilization, and staining with Alexafluor-568-phalloidin to visualize F-actin filaments. Cells were imaged in the green (left column, GFP Signal) and red (right column, F-actin Signal) channels. Scale bar = 20 µm. wt = wild-type. **b** Anti-GFP immunoblot on lysates from NIH-3T3 cells transiently transfected with GFP or FLNaABD-GFP ± N-terminal truncations. Vinculin was used as a loading control. **c** Micrographs of fibroblasts transfected with GFP or FLNaABD-GFP constructs containing ABS-N mutations, prepared and imaged as in (**a**). Scale bar = 20 µm. **d** Anti-GFP immunoblot on lysates from NIH-3T3 cells transiently transfected with GFP or FLNaABD-GFP ± ABS-N mutations. Vinculin was used as a loading control.

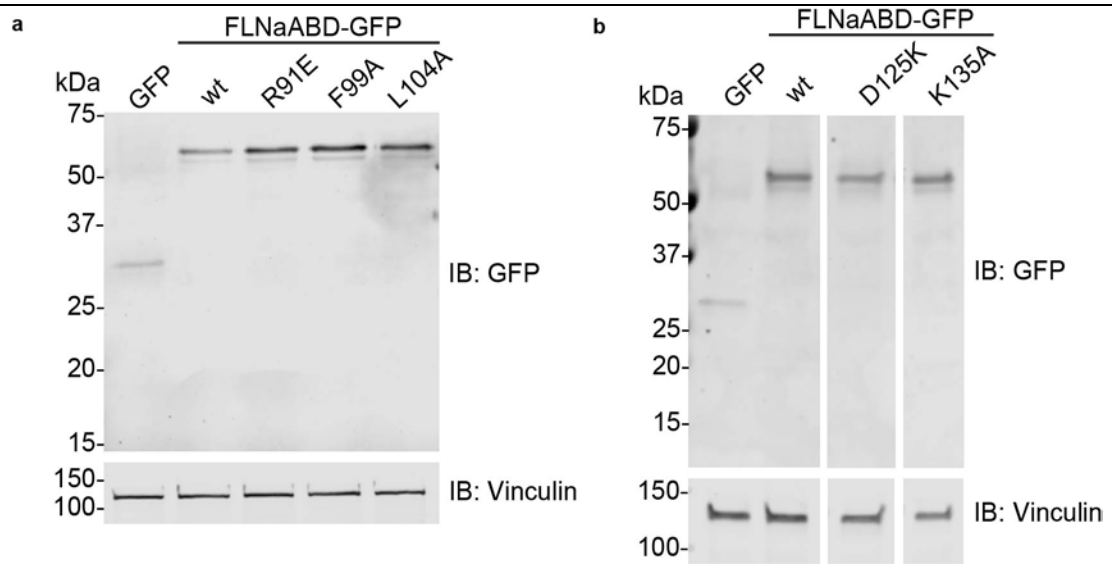

Supplementary Figure 3

Immunoblotting of ABS2' and ABS2 mutant FLNaABDs.

a Anti-GFP immunoblot on lysates from NIH-3T3 cells transiently transfected with GFP or FLNaABD-GFP ± ABS2' mutations. Vinculin was used as a loading control. wt = wild-type. **b** Anti-GFP immunoblot on lysates from NIH-3T3 cells transiently transfected with GFP or FLNaABD-GFP ± ABS2 mutations. Vertical separations between panels indicate the exclusion of non-relevant lane samples from the same gel. Vinculin was used as a loading control.

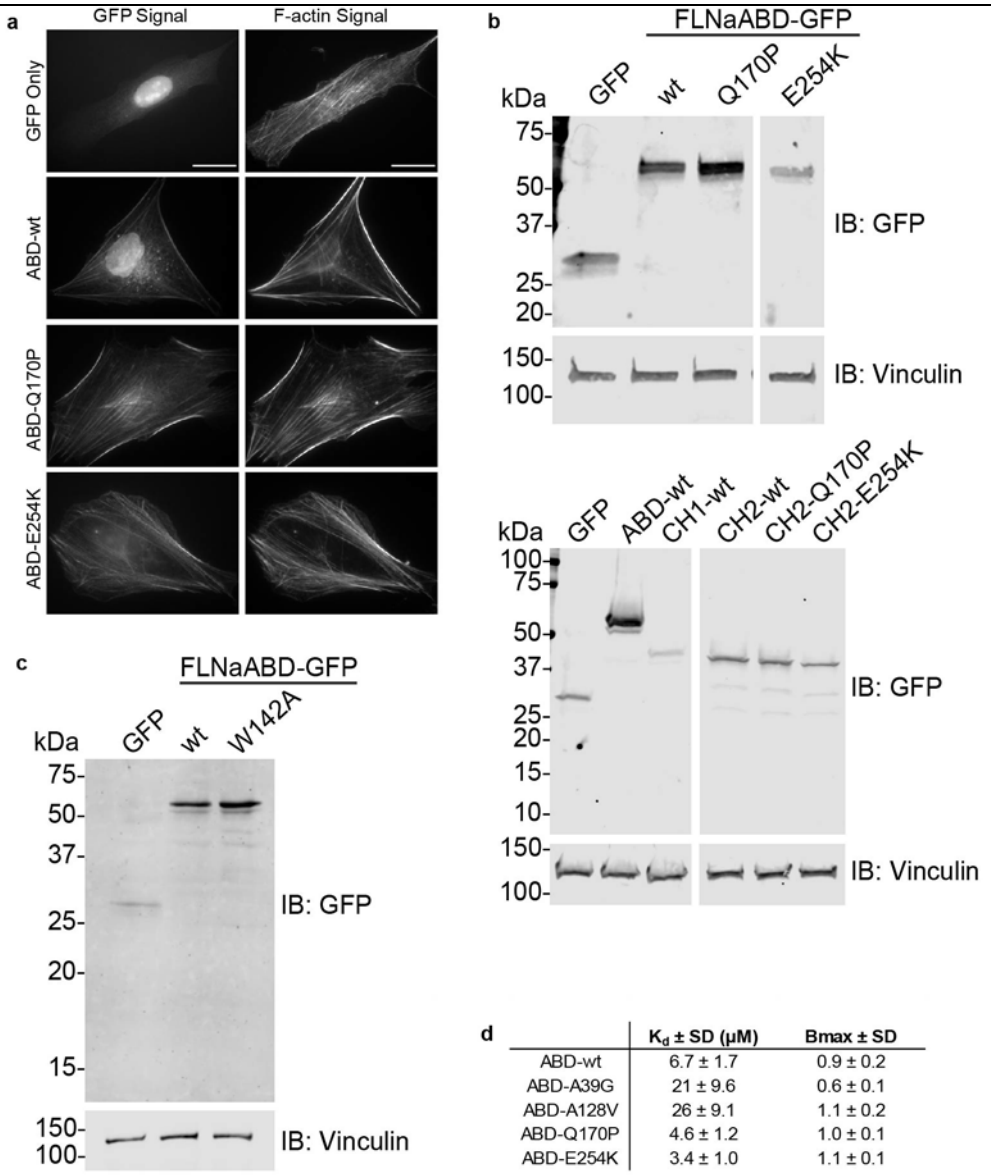

	K_d ± SD (μM)	Bmax ± SD
ABD-wt	6.7 ± 1.7	0.9 ± 0.2
ABD-A39G	21 ± 9.6	0.6 ± 0.1
ABD-A128V	26 ± 9.1	1.1 ± 0.2
ABD-Q170P	4.6 ± 1.2	1.0 ± 0.1
ABD-E254K	3.4 ± 1.0	1.1 ± 0.1

Supplementary Figure 4

OPDSD-associated mutations increase FLNaABD binding to F-actin.

a Micrographs of mouse NIH-3T3 fibroblasts transiently transfected with GFP or FLNaABD-GFP ± the Q170P or E254K mutation after fixation, permeabilization, and staining with Alexafluor-568-phalloidin to visualize actin filaments. Cells were imaged in the green (left column, GFP Signal) and red (right column, F-actin Signal) channels. Scale bar = 20 μm. wt = wild-type. **b** Top and bottom, anti-GFP immunoblots on lysates from NIH-3T3 cells transiently transfected with GFP, FLNaABD-GFP or isolated FLNaCH-GFP domains ± the Q170P or E254K mutation. Vinculin was used as a loading control. Vertical separations between panels indicate the exclusion of non-relevant lane samples from the same gel. **c** Anti-GFP immunoblot on lysates from NIH-3T3 cells transiently transfected with GFP, FLNaABD-GFP or FLNaABD-W142A-GFP. Vinculin was used as a loading control. **d** Table summarizing apparent dissociation constants (K_d, μM) and Bmax (molar ratio ABD:actin) from co-sedimentation assays with purified wt or mutant 6x-His-FLNaABD proteins, ± standard deviation.

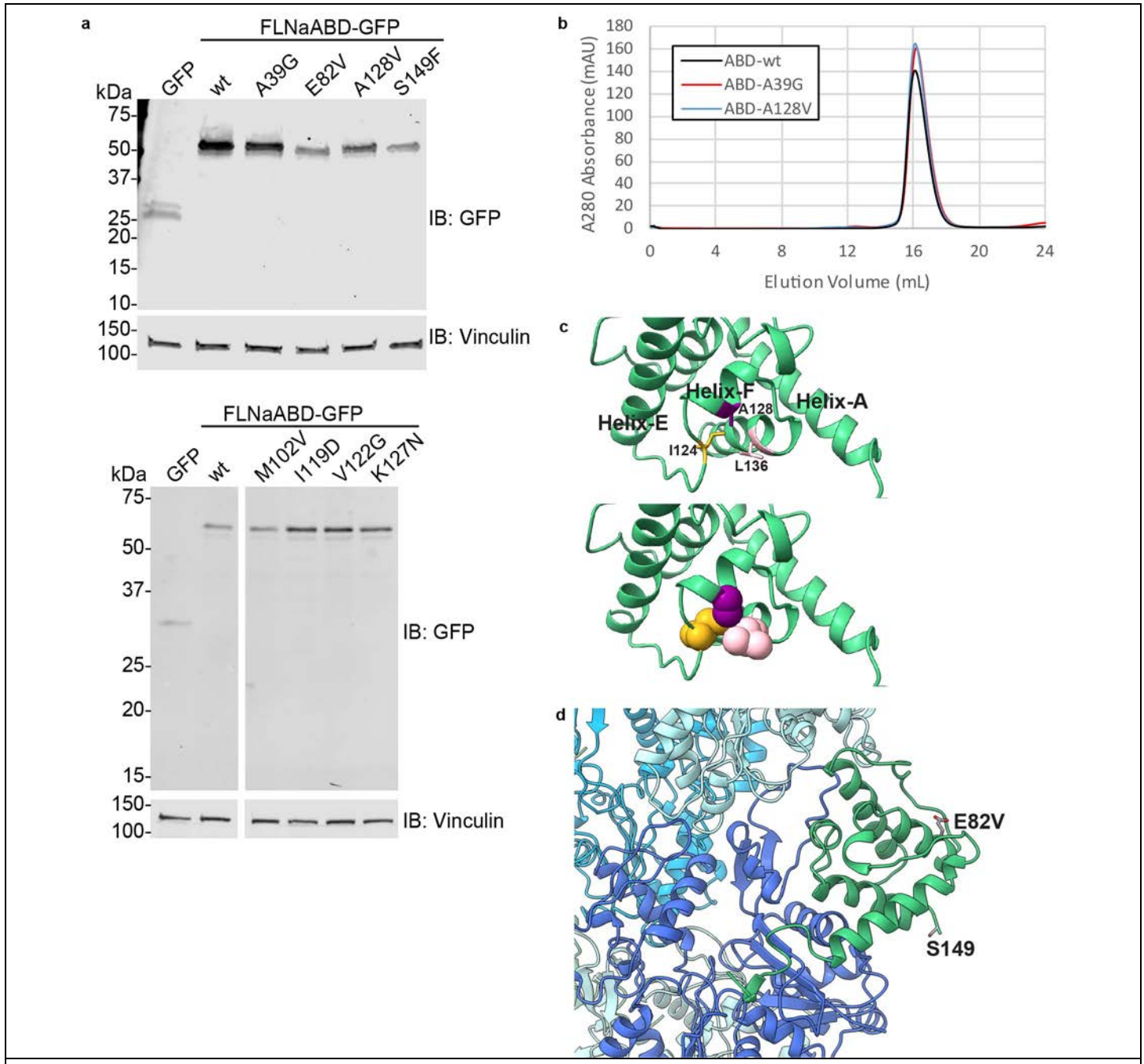

Supplementary Figure 5

Immunoblotting and size-exclusion chromatography of FLNaABD with PVNH-associated mutations.

a Top and bottom, anti-GFP immunoblots on lysates from NIH-3T3 cells transiently transfected with GFP or FLNaABD-GFP ± PVNH mutations. Vinculin was used as a loading control. wt = wild-type. **b** Analytical size-exclusion chromatography of purified bacterially expressed 6x-His-FLNaABD-wt, -A39G, or -A128V. Protein concentration was measured by UV absorbance at 280 nm (arbitrary units, mAU). **c** Top, the FLNa residue A128 is located in Helix-F of the CH1 domain and does not contact actin, though its mutation to valine would likely perturb this short helix (see space-filling models, bottom) which contains important actin-binding residues (not shown) and result in a loss of actin binding. **d** The FLNaCH1 residues E82 and S149 (mutated in PVNH) are situated far from F-actin binding sites in the actin-bound cryo-EM structure.

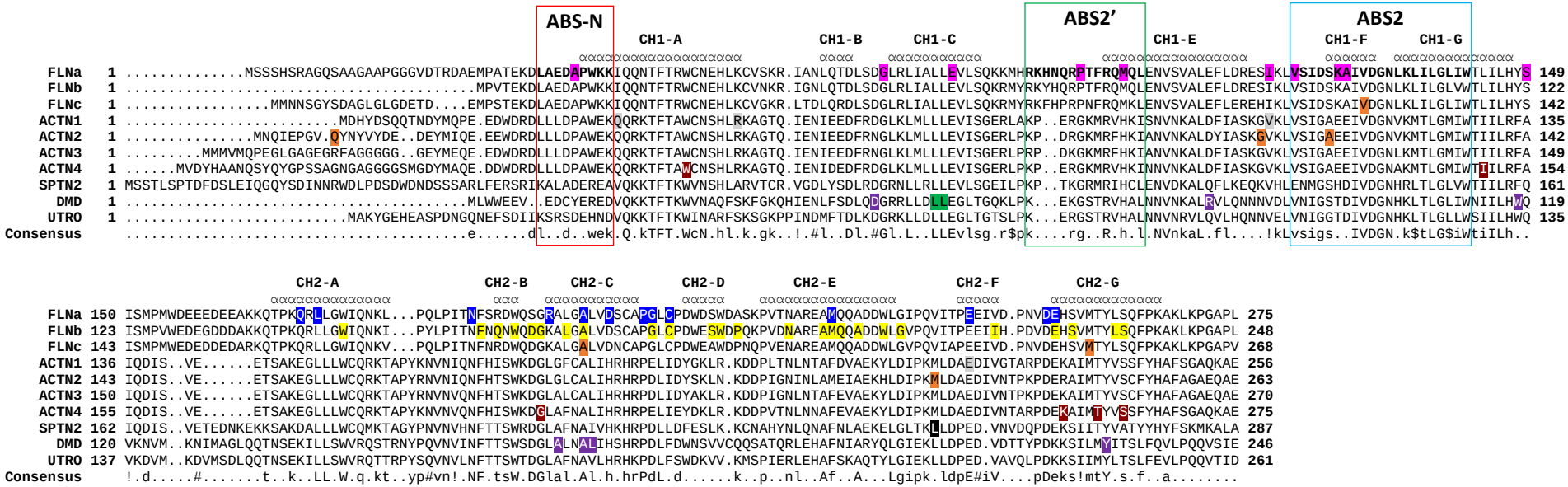

Supplementary Note. Protein sequence alignment of selected human ABDs.

ABDs of FLNa (UniProt Accession Code O21333), FLNb (O75369), FLNc (Q14315), α-actinin 1 (ACTN1 P12814), ACTN2 (P35609), ACTN3 (Q08043), ACTN4 (O43707), β-III-spectrin (SPTN2 O15020), dystrophin (DMD P11532), utrophin (UTRO P46939) were aligned using MultAlin[1]. F-actin-interacting regions in FLNa are bolded and boxed (red = ABS-N, green = ABS2', blue = ABS2). Secondary structure α-helical elements from FLNa are shown above the alignment as α's and are labeled with the corresponding CH domain and helix letter identifier. The consensus sequence indicates high conservation (>90%, upper-case amino acid code abbreviation), low conservation (50-90%, lower-case abbreviation), or molecular group conservation (! = I or V, $ = L or M, % = F or Y, # = N, D, Q, or E). Highlighted residues indicate disease-associated point mutations at this position: magenta = PVNH[2–11], blue = OPDSD[12–17], yellow = Larsen syndrome, atelosteogenesis I and III and Boomerang dysplasia disorders[18–23], orange = distal and cardiomyopathies[24–29], grey = macrothrombocytopenia[30], maroon = focal segmental glomerulosclerosis[31–33], black = spinocerebellar ataxia type 5[34], green = Duchenne's muscular dystrophy[35,36], purple = Becker muscular dystrophy[37–41].

Supplementary Note References

1. Corpet, F. Multiple sequence alignment with hierarchical clustering. *Nucleic Acids Res.* **16,** 10881–10890 (1988).
2. Solé, G. *et al.* Bilateral periventricular nodular heterotopia in France: Frequency of mutations in FLNA, phenotypic heterogeneity and spectrum of mutations. *J. Neurol. Neurosurg. Psychiatry* **80,** 1394–1398 (2009).
3. Sheen, V. L. *et al.* Filamin A mutations cause periventricular heterotopia with Ehlers-Danlos syndrome. *Neurology* **64,** 254—262 (2005).
4. Gómez-Garre, P. *et al.* Ehlers-Danlos syndrome and periventricular nodular heterotopia in a Spanish family with a single FLNA mutation. *J. Med. Genet.* **43,** 232–237 (2006).
5. Guerrini, R. *et al.* Germline and mosaic mutations of FLN1 in men with periventricular heterotopia. *Neurology* **63,** 51–56 (2004).
6. Moro, F. *et al.* Familial periventricular heterotopia: missense and distal truncating mutations of the FLN1 gene. *Neurology* **58,** 916–921 (2002).
7. De Wit, M. C. Y. *et al.* Combined cardiological and neurological abnormalities due to filamin A gene mutation. *Clin. Res. Cardiol.* **100,** 45–50 (2011).
8. Liu, W. *et al.* Sporadic periventricular nodular heterotopia: Classification, phenotype and correlation with Filamin A mutations. *Epilepsy Res.* **133,** 33–40 (2017).
9. Reinstein, E. *et al.* Vascular and connective tissue anomalies associated with X-linked periventricular heterotopia due to mutations in Filamin A. *Eur. J. Hum. Genet.* **21,** 494–502 (2013).
10. Parrini, E. *et al.* Periventricular heterotopia : phenotypic heterogeneity and correlation with Filamin A mutations. *Brain* **72,** 1892–1906 (2006).
11. Lange, M. *et al.* 47 patients with FLNA associated periventricular nodular heterotopia. *Orphanet J. Rare Dis.* **10,** 134 (2015).
12. Robertson, S. P. *et al.* Localized mutations in the gene encoding the cytoskeletal protein filamin A cause diverse malformations in humans. *Nat. Genet.* **33,** 487–491 (2003).
13. Moutton, S. *et al.* Otopalatodigital spectrum disorders: refinement of the phenotypic and mutational spectrum. *J. Hum. Genet.* **61,** 693–699

(2016).

14. Naudion, S. *et al.* Fetal phenotypes in otopalatodigital spectrum disorders. *Clin. Genet.* **89,** 371–377 (2016).

15. Robertson, S. P. *et al.* Frontometaphyseal Dysplasia: Mutations in FLNA and Phenotypic Diversity. *Am. J. Med. Genet. A* **140A,** 1726–1736 (2006).

16. Mariño-Enríquez, A., Lapunzina, P., Robertson, S. P. & Rodríguez, J. I. Otopalatodigital Syndrome Type 2 in Two Siblings With a Novel Filamin A 629G-T Mutation: Clinical, Pathological, and Molecular Findings. *Am. J. Med. Genet. A* **143A,** 2106–2112 (2007).

17. Parrini, E. *et al.* Familial periventricular nodular heterotopia, epilepsy and Melnick-Needles Syndrome caused by a single FLNA mutation with combined gain-of-function and loss-of-function effects. *J. Med. Genet.* **52,** 405–412 (2015).

18. Farrington-Rock, C. *et al.* Mutations in two regions of FLNB result in atelosteogenesis I and III. *Hum. Mutat.* **27,** 705–710 (2006).

19. Jeon, G. W. *et al.* Identification of a de novo heterozygous missense FLNB mutation in lethal atelosteogenesis type i by exome sequencing. *Ann. Lab. Med.* **34,** 134–138 (2014).

20. Bicknell, L. S. *et al.* Mutations in FLNB cause boomerang dysplasia. *J. Med. Genet.* **42,** e43 (2005).

21. Daniel, P. B. *et al.* Disease-associated mutations in the actin-binding domain of filamin B cause cytoplasmic focal accumulations correlating with disease severity. *Hum. Mutat.* **33,** 665–673 (2012).

22. Krakow, D. *et al.* Mutations in the gene encoding filamin B disrupt vertebral segmentation, joint formation and skeletogenesis. *Nat. Genet.* **36,** 405–410 (2004).

23. Bicknell, L. S. *et al.* A molecular and clinical study of Larsen syndrome caused by mutations in FLNB. *J. Med. Genet.* **44,** 89–98 (2007).

24. Valdés-Mas, R. *et al.* Mutations in filamin C cause a new form of familial hypertrophic cardiomyopathy. *Nat. Commun.* **5,** 5326 (2014).

25. Duff, R. M. *et al.* Mutations in the N-terminal actin-binding domain of filamin C cause a distal myopathy. *Am. J. Hum. Genet.* **88,** 729–740 (2011).

26. Mohapatra, B. *et al.* Mutations in the muscle LIM protein and α-actinin-2 genes in dilated cardiomyopathy and endocardial fibroelastosis. *Mol. Genet. Metab.* **80,** 207–215 (2003).

27. Theis, J. L. *et al.* Echocardiographic-determined septal morphology in Z-disc hypertrophic cardiomyopathy. *Biochem. Biophys. Res. Commun.* **351,** 896–902 (2006).

28. Bagnall, R. D., Molloy, L. K., Kalman, J. M. & Semsarian, C. Exome sequencing identifies a mutation in the ACTN2 gene in a family with idiopathic ventricular fibrillation, left ventricular noncompaction, and sudden death. *BMC Med. Genet.* **15,** 99 (2014).

29. Girolami, F. *et al.* Novel alpha-actinin 2 variant associated with familial hypertrophic cardiomyopathy and juvenile atrial arrhythmias. *Circ. Cardiovasc. Genet.* **7,** 741–750 (2014).

30. Kunishima, S. *et al.* ACTN1 mutations cause congenital macrothrombocytopenia. *Am. J. Hum. Genet.* **92,** 431–438 (2013).

31. Weins, A. *et al.* Mutational and Biological Analysis of -Actinin-4 in Focal Segmental Glomerulosclerosis. *J. Am. Soc. Nephrol.* **16,** 3694–3701 (2005).

32. Kaplan, J. M. *et al.* Mutations in ACTN4, encoding alpha-actinin-4, cause familial focal segmental glomerulosclerosis. *Nat. Genet.* **24,** 251–256 (2000).

33. Bartram, M. P. *et al.* Three-layered proteomic characterization of a novel ACTN4 mutation unravels its pathogenic potential in FSGS. *Hum. Mol. Genet.* **25,** 1152–1164 (2015).

34. Ikeda, Y. *et al.* Spectrin mutations cause spinocerebellar ataxia type 5. *Nat. Genet.* **38,** 184–190 (2006).

35. Juan-Mateu, J. *et al.* Interplay between DMD Point Mutations and Splicing Signals in Dystrophinopathy Phenotypes. *PLoS One* **8,** e59916 (2013).

36. Prior, T. W. *et al.* A missense mutation in the dystrophin gene in a Duchenne muscular dystrophy patient. *Nat. Genet.* **4,** 357–360 (1993).

37. Kesari, A. *et al.* Integrated DNA, cDNA and protein studies in Becker muscular dystrophy show high exception to the reading frame rule. *Hum.*

Mutat. **29,** 728–737 (2008).

38. Hamed, S. A., Sutherland-Smith, A. J., Gorospe, J. R. M., Kendrick-Jones, J. & Hoffman, E. P. DNA sequence analysis for structure/function and mutation studies in Becker muscular dystrophy. *Clin. Genet.* **68,** 69–79 (2005).

39. Magri, F. *et al.* Clinical and molecular characterization of a cohort of patients with novel nucleotide alterations of the Dystrophin gene detected by direct sequencing. *BMC Med. Genet.* **12,** 37 (2011).

40. Roberts, R. G., Gardner, R. J. & Bobrow, M. Searching for the 1 in 2,400,000: A review of Dystrophin Gene Point Mutations. *Hum. Mutat.* **4,** 1–11 (1994).

41. Norwood, F. L. M., Sutherland-Smith, A. J., Keep, N. H. & Kendrick-Jones, J. The structure of the N-terminal actin-binding domain of human dystrophin and how mutations in this domain may cause Duchenne or Becker muscular dystrophy. *Structure* **8,** 481–491 (2000).